# Global ocean biogeochemistry model HAMOCC: Model architecture and performance as component of the MPI-Earth system model in different CMIP5 experimental realizations

Tatiana Ilyina,[1] Katharina D. Six,[1] Joachim Segschneider,[1] Ernst Maier-Reimer,[1] Hongmei Li,[1] and Ismael Núñez-Riboni[1,2]

[1] Ocean biogeochemistry is a novel standard component of fifth phase of the Coupled Model Intercomparison Project (CMIP5) experiments which project future climate change caused by anthropogenic emissions of greenhouse gases. Of particular interest here is the evolution of the oceanic sink of carbon and the oceanic contribution to the climate-carbon cycle feedback loop. The Hamburg ocean carbon cycle model (HAMOCC), a component of the Max Planck Institute for Meteorology Earth system model (MPI-ESM), is employed to address these challenges. In this paper we describe the version of HAMOCC used in the CMIP5 experiments (HAMOCC 5.2) and its implementation in the MPI-ESM to provide a documentation and basis for future CMIP5-related studies. Modeled present day distributions of biogeochemical variables calculated in two different horizontal resolutions compare fairly well with observations. Statistical metrics indicate that the model performs better at the ocean surface and worse in the ocean interior. There is a tendency for improvements in the higher resolution model configuration in representing deeper ocean variables; however, there is little to no improvement at the ocean surface. An experiment with interactive carbon cycle driven by emissions of $CO_2$ produces a 25% higher variability in the oceanic carbon uptake over the historical period than the same model forced by prescribed atmospheric $CO_2$ concentrations. Furthermore, a climate warming of 3.5 K projected at atmospheric $CO_2$ concentration of four times the preindustrial value, reduced the atmosphere-ocean $CO_2$ flux by 1 GtC yr$^{-1}$. Overall, the model shows consistent results in different configurations, being suitable for the type of simulations required within the CMIP5 experimental design.

## 1. Introduction

[2] As atmospheric concentrations of carbon dioxide ($CO_2$) rise, questions regarding the evolution of the oceanic carbon sink and climate-carbon cycle feedbacks receive augmented public and scientific attention. The design of the fifth phase of the Coupled Model Intercomparison Project (CMIP5) includes, inter alia, simulations of ocean biogeochemistry and its role in Earth's climate and requires reporting seawater biogeochemical data to the project's standard database Earth system grid (ESG). The ultimate objective of this activity is to address climate-related scientific demands in the preparation of the Fifth Assessment Report (AR5) of the Intergovernmental Panel on Climate Change (IPCC). Together with ESMs from other modeling groups, the Earth system model of the Max Planck Institute for Meteorology (MPI-ESM) (M. Giorgetta et al., Climate change from 1850 to 2100 in MPI-ESM CMIP5 simulations, submitted to *Journal of Advances in Modeling Earth Systems*, 2012, hereinafter referred to as Giorgetta et al., submitted manuscript, 2012) takes part in the CMIP5 climate model experiment. Ocean biogeochemistry in MPI-ESM is represented by the Hamburg Ocean Carbon Cycle (HAMOCC) model. HAMOCC, embedded into the MPI's Ocean General Circulation Model (MPIOM) (J. Jungclaus et al., Characteristics of the ocean simulations in MPIOM, the ocean component of MPI-Earth system model, submitted to *Journal*

---

[1]The Ocean in the Earth System, Max Planck Institute for Meteorology, Hamburg, Germany.

[2]Now at Johann Heinrich von Thünen-Institute, Institute of Sea Fisheries, Hamburg, Germany.

*of Advances in Modeling Earth Systems*, 2012, hereinafter referred to as Jungclaus et al., submitted manuscript, 2012), simulates the oceanic cycles of carbon and other biogeochemical elements. It has first been used with interactive carbon cycle in the coupled ocean-atmosphere-land system stands for community earth system models (COSMOS) [*Friedlingstein et al.*, 2006; *Jungclaus et al.*, 2010).

[3] HAMOCC has been initially developed to study the role of oceanic transport and storage of carbon in the climate system in the original work by *Maier-Reimer* [1984] and *Maier-Reimer and Hasselmann* [1987]. The modeling concept in this approach was to transport inorganic carbon with a three-dimensional (3-D) flow field calculated by the large scale geostrophic (LSG, *Maier-Reimer et al.* [1993]) ocean general circulation model (OGCM). Further milestones in HAMOCC development involved incorporation of the first-order biological processes including phosphate and the oxygen cycle [*Bacastow and Maier-Reimer*, 1990; *Maier-Reimer*, 1993]. Later, the marine food web has been defined by nutrients, phytoplankton, zooplankton, detritus (an extended NPZD-type approach) and dissolved organic matter (DOM) as described in *Six and Maier-Reimer* [1996]. In its current version, colimitation by major macronutrients and micronutrients, i.e., phosphate, nitrate, and dissolved iron, is considered. The model has been expanded with the cycles of other biogeochemical tracers, such as species of nitrogen (including the greenhouse gas $N_2O$) and dimethylsulfide (DMS, an aerosol precursor) [*Kloster et al.*, 2006, 2007; *Six and Maier-Reimer*, 2006]. Additionally, a sediment module has been designed to address the biogeochemistry of pore-water tracers and solid constituents in the upper bioturbated sediments [*Heinze et al.*, 1999; *Heinze and Maier-Reimer*, 1999]. In this way, HAMOCC describes cycles of biogeochemical elements in the ocean water column and sediment; it also calculates fluxes of tracers between these two compartments and at the air-sea interface.

[4] The major focus of the model development has been on the role of ocean biogeochemistry in the Earth's climate over timescales ranging from seasons to thousands of years. As such, a good representation of large-scale tracer gradients was brought into focus of the modeling effort, rather than details of surface ocean ecosystem processes, as for instance the temporal variation of chlorophyll concentrations. The modeling strategy aimed at reproducing the distributions of biogeochemical parameters without regional tuning or temporal adjustments toward observations, solely depending on the numerical description of the biogeochemical processes and the oceanic flow field. HAMOCC has served as a prototype for other global ocean biogeochemical models, such as the model PISCES [*Aumont et al.*, 2003] and has been employed with other OGCMs, e.g., the isopycnic ocean model MICOM as used in the Norwegian Earth system model [*Assmann et al.*, 2010; *Tjiputra et al.*, 2012]. HAMOCC has been used in a number of pioneering studies on the ocean carbon cycle [e.g., *Winguth et al.*, 1994; *Maier-Reimer and Hasselmann*, 1987; *Heinze*, 2004; *Wetzel et al.*, 2005; *Kloster et al.*, 2006,

2007; *Ilyina et al.*, 2009, 2010]. The model participated in major model intercomparison initiatives which investigated different aspects of the carbon cycle and climate-carbon cycle feedbacks [e.g., *Orr et al.*, 2005; *Friedlingstein et al.*, 2006; *Najjar et al.*, 2007; *Schneider et al.*, 2008; *Steinacher et al.*, 2010; *Le Clainche et al.*, 2010; *Roy et al.*, 2011; *Duteil et al.*, 2012].

[5] This paper aims at providing users of MPI-ESM CMIP5 data with a documentation of the employed biogeochemistry model HAMOCC, a first comparison with present-day observations and first results from selected experiments. More general, it gives some insights into the particular requirements when using the biogeochemistry model as a component of an Earth system model. A detailed technical description of the model version HAMOCC 5.1 is given in *Maier-Reimer et al.* [2005], and single components of the model that have been updated since then are described in the papers cited above and in the following sections. This current HAMOCC version is referred to as HAMOCC 5.2. In sections 2 and 3 of this paper, we update the model description with a focus on the operation of HAMOCC 5.2 as a component of the MPI-ESM as used in CMIP5 experiments. In section 4, we then assess model performance by comparison with present-day observations for the historical experiments (from preindustrial up to present day) and describe the impact of the two different model resolutions on the representation of the present-day ocean biogeochemistry. In further sections of the paper, we describe the performance of HAMOCC in a subset of CMIP5 experiments. In section 5, we compare two experiments, one with prescribed atmospheric $pCO_2$ and one with an interactive (free) carbon cycle forced by emissions. As part of CMIP5, historical runs and idealized projection runs (1% per year increase in atmospheric $CO_2$ concentration up to 4 times the preindustrial concentration and an abrupt quadrupling of atmospheric $CO_2$ content) have been performed. In section 6, we analyze model behavior in response to idealized greenhouse gas (GHG) projections, and we conclude in section 7.

## 2. Model Description

[6] Ocean biogeochemistry as part of the Earth system controls the uptake of atmospheric $CO_2$ and storage of carbon in the ocean on the timescale from days to millennia. The longest timescales of the marine carbon cycle are related to sediment and weathering processes. Hence, in this model description we divide processes simulated by HAMOCC into three major categories. These are biogeochemistry of the water column (including organic and inorganic carbon cycle processes), sediment biogeochemistry, and interactions with the atmosphere. The key components of the model HAMOCC are given in Figure 1. The model in the configuration described here has 17 state variables calculated prognostically in the water column (listed in Table 1) and 12 state variables in the sediment. Modifications in the model version HAMOCC 5.2 following the technical report by *Maier-Reimer et al.* [2005] which are incorporated in the CMIP5 experimental
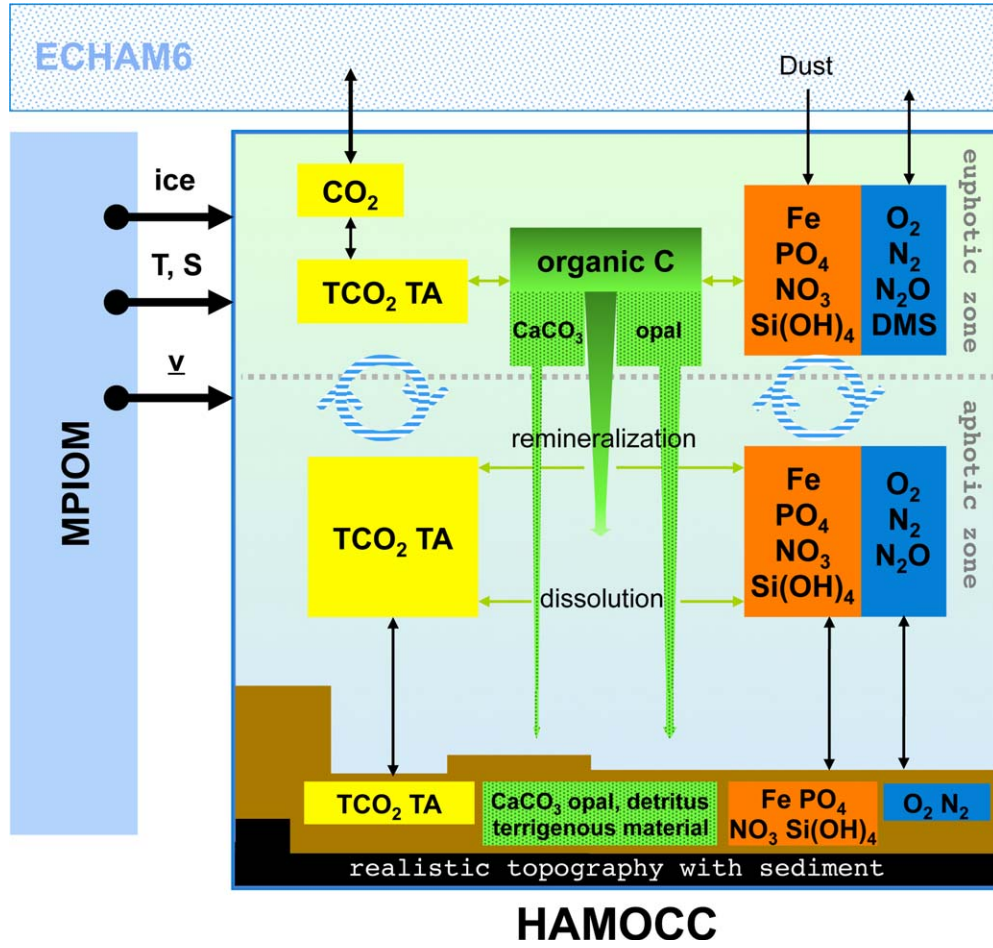
**Figure 1.** A schematic overview of the global ocean biogeochemistry model HAMOCC.

design are described in the following sections. These include: correction of temperature fit in air-sea exchange [*Gröger and Mikolajewicz*, 2011], temperature-dependent photosynthesis, sulphate reduction, iron as pore water tracer (in the sediment module), remineralization in the

**Table 1.** List of State Variables Treated Prognostically in the Model HAMOCC

| Acronym | Name | Unit |
|---------|------|------|
| $TCO_2$ | Dissolved inorganic carbon | $kmol\ C\ m^{-3}$ |
| TA | Total alkalinity | $kmol\ C\ m^{-3}$ |
| $PO_4$ | Phosphate | $kmol\ P\ m^{-3}$ |
| $NO_3$ | Nitrate | $kmol\ N\ m^{-3}$ |
| Si | Silicate | $kmol\ Si\ m^{-3}$ |
| Fe | Dissolved bioavailable iron | $kmol\ Fe\ m^{-3}$ |
| $O_2$ | Dissolved oxygen | $kmol\ O_2\ m^{-3}$ |
| Phy | Phytoplankton | $kmol\ P\ m^{-3}$ |
| Zoo | Zooplankton | $kmol\ P\ m^{-3}$ |
| DOM | Dissolved organic matter | $kmol\ C\ m^{-3}$ |
| Det | Detritus | $kmol\ P\ m^{-3}$ |
| Opal | Opal shells | $kmol\ Si\ m^{-3}$ |
| $CaCO_3$ | Calcium carbonate shells | $kmol\ C\ m^{-3}$ |
| Dust | Terrigenous material | $kg\ m^{-3}$ |
| $N_2$ | Dinitrogen | $kmol\ N\ m^{-3}$ |
| $N_2O$ | Dinitrous oxide | $kmol\ N\ m^{-3}$ |
| DMS | Dimethylsulfide | $kmol\ S\ m^{-3}$ |

euphotic layer, compensation of loss of shell material (silicate, alkalinity, and dissolved inorganic carbon) to sediment during long spin-up runs, changes in alkalinity during denitrification and nitrogen fixation, and output routines to address CMIP5 requirements.

### 2.1. Water Column Biogeochemistry

[7] All biogeochemical tracer concentrations are distributed by the 3-D flow field computed in the OGCM MPIOM (section 3.1). Freshwater fluxes from river runoff and precipitation (evaporation) decrease (increase) the concentration of biogeochemical tracers in the same manner as for salinity. Additionally, tracer concentrations vary due to biogeochemical processes and, for selected tracers, also due to air-sea exchanges. Changes in tracer concentrations are described by the differential equation of transport.

$$\frac{\partial C^i}{\partial t} + \mathbf{V}\nabla C^i - DC^i = \Sigma_k \Psi_k^i \left( C_k, C^i \right) + \Psi_{\text{air-sea}} + \Psi_{\text{sedflux}},$$

$$(1)$$

where $\mathbf{V}$ is the 3-D advection vector, $D$ the diffusion operator, and $\Psi$ refers to the source and sink operators

for biogeochemical processes, fluxes across the air-sea interface, and interactions with the sediment. In the following, we describe the processes summarized by $\Psi$ in equation (1) without considering the term for advection and diffusion. All parameters and rates used in the model are given in Table 2.

### 2.1.1. Organic Carbon Cycle

[8] Marine biology dynamics in HAMOCC is based on an extended NPZD model (as described in *Six and Maier-Reimer* [1996]), which connects biogeochemical cycles and trophic levels through the uptake of nutrients and remineralization of organic matter. The NPZD

**Table 2.** List of Constants in the Model HAMOCC

| Symbol | Variable | Value | Units |
|---|---|---|---|
| | Phytoplankton | | |
| $\alpha$ | Initial slope of $P$ versus $I$ curve | 0.02 | $d^{-1} (W\,m^{-2})^{-1}$ |
| $k_r$ | Mean light attenuation coefficient of water for $v < 580$ nm | 0.35 | $m^{-1}$ |
| $k_w$ | Mean light attenuation coefficient of water for $v \geq 580$ nm | 0.03 | $m^{-1}$ |
| $k_c$ | Light attenuation coefficient of chlorophyll | 0.04 | $m^{-1} (kmol\,P\,m^{-3})^{-1}$ |
| $\sigma$ | Dividing PAR domain at 580 nm | 0.4 | |
| $\mu_{phy}$ | Growth rate | 0.6 | $d^{-1}$ |
| $R_{C:Chl}$ | C:Chl ratio of phytoplankton | 60 | $g\,C\,g\,Chl^{-1}$ |
| $Phy_{min}$ | Min. concentration of phytoplankton | 1E-11 | $kmol\,P\,m^{-3}$ |
| $\lambda_{phy}$ | Mortality rate | 0.008 | $d^{-1}$ |
| $\beta_{phy}$ | Exudation rate | 0.03 | $d^{-1}$ |
| | Zooplankton | | |
| $\mu_{zoo}$ | Max. grazing rate | 1 | $d^{-1}$ |
| $K_{zoo}$ | Half-saturation constant for grazing | 4 E-8 | $kmol\,P\,m^{-3}$ |
| $Zoo_{min}$ | Min. concentration of zooplankton | 1E-11 | $kmol\,P\,m^{-3}$ |
| $1 - \epsilon_{zoo}$ | Fraction of grazing egested | 1–0.8 | |
| $\omega_{zoo}$ | Assimilation efficiency | 0.6 | |
| $\lambda_{zoo}$ | Mortality rate | 3E6 | $d^{-1} (kmol\,P\,m^{-3})^{-1}$ |
| $\beta_{zoo}$ | Excretion rate | 0.06 | $d^{-1}$ |
| $1 - \epsilon_{can}$ | Fraction of carnivores grazing egested | 1–0.95 | |
| $w_{det}$ | Sinking speed of detritus | 5 | $d^{-1}$ |
| | Nutrients | | |
| $K_{PO_4}$ | Half-saturation constant for $PO_4$ uptake | 1E-8 | $kmol\,P\,m^{-3}$ |
| $K_{NO_3}$ | Half-saturation constant for $NO_3$ uptake | 1.6 E-7 | $kmol\,N\,m^{-3}$ |
| $K_{Fe}$ | Half-saturation constant for Fe uptake | 0.0036 | $nmol\,Fe\,m^{-3}$ |
| $R_{dust}$ | Ratio of bioavailable iron in Dust | 6.26 E-6 | $kmol\,Fe\,kg^{-1}$ |
| $\lambda_{Fe}$ | Complexation rate for Fe | | $d^{-1}$ |
| $Fe_{crit}$ | Critical Fe concentration of complexation | 0.6 | $nmol\,L^{-1}$ |
| $\mu_{cyan}$ | $N_2$ fixation rate | 0.005 | $d^{-1}$ |
| $R_{denit}$ | Ratio of mol N consumed per mol P in detritus being denitrified | 137.6 | $kmol\,N\,kmol\,P^{-1}$ |
| $O_{2crit}$ | Critical $O_2$ concentration of remineralization | 0.5 | $\mu mol\,L^{-1}$ |
| $\lambda_{det}$ | Remineralization rate | 0.025 | $d^{-1}$ |
| $\lambda_N$ | Denitrification rate | 0.005 | $d^{-1}$ |
| $\lambda_S$ | Sulphate reduction rate | 0.005 | $d^{-1}$ |
| $\lambda_{N_2O}$ | Denitrification rate for $N_2O$ | 0.01 | $d^{-1}$ |
| $r_{N_2O}$ | Mol N produced per mol $O_2$ at $N_2O$ remineralization | 1E-4 | $kmol\,N\,kmol\,O_2^{-1}$ |
| $R_{N_2O}$ | Mol N consumed per mol P in detritus denitrified by $N_2O$ | 344 | $kmol\,N\,kmol\,P^{-1}$ |
| | Dissolved Organic Matter | | |
| $\lambda_{dom}$ | Remineralization rate | 0.004 | $d^{-1}$ |
| | Shell Material | | |
| $K_{SiO}$ | Half-saturation constant for $Si(OH)_4$ uptake | 1E-6 | $kmol\,Si\,m^{-3}$ |
| $R_{Si:P}$ | Opal:P uptake ratio | 25 | $mol\,Si\,mol\,P^{-1}$ |
| $R_{Ca:P}$ | $CaCO_3$:P uptake ratio | 20 | $mol\,C\,mol\,P^{-1}$ |
| $w_{opal}$ | Sinking speed of opal shells | 30 | $d^{-1}$ |
| $w_{calc}$ | Sinking speed for calcite shells | 30 | $d^{-1}$ |
| $\lambda_{opal}$ | Opal dissolution rate | 0.01 | $d^{-1}$ |
| $\lambda_{calc}$ | Calcite dissolution rate | 0.075 | $d^{-1}$ |
| | Dimethyl Sulfide (DMS) | | |
| $\gamma_{photo}$ | Photodestruction | 0.0075 | $(W\,m^{-2})^{-1}\,d^{-1}$ |
| $\gamma_{bac}$ | Temperature-dependent bacterial consumption rate | 0.0096 | $°C^{-1}\,d^{-1}$ |
| $\gamma_c$ | Production by calcifiers | 0.1345 | $kmol\,S\,(kmol\,C)^{-1}\,d^{-1}$ |
| $\gamma_d$ | Production by silicifiers | 0.0137 | $kmol\,S\,(kmol\,C)^{-1}\,d^{-1}$ |
| $k_{dms}$ | Microbial half saturation | 1E-8 | $kmol\,S\,m^{-3}$ |

module consists of seven compartments being nutrients (phosphate, nitrate and iron), phytoplankton, zooplankton, DOM, and sinking particulate organic matter (detritus). All organic compounds have identical nutrient and oxygen composition following the Redfield ratio concept [*Takahashi et al.*, 1985] with the constant elemental stoichiometric ratio for carbon (C:N:P:$O_2$ = 122:16:1:−172) and the micronutrient iron (Fe:P = 366 E-6:1).

[9] HAMOCC5.2 has only one phytoplankton state variable as basis for marine primary production. Plankton concentration is then subdivided into opal - and calcium carbonate-producing fractions as basis for shell production (see section 2.1.3 for details). While capturing the most relevant features of the effects of biology on the ocean carbon cycle (i.e., the export flux of organically fixed carbon out of the euphotic zone), such parameterization may underestimate the turnover rates of the biological system in the euphotic zone (i.e., gross primary production). These turnover fluxes, however, have only local (in space and time) influences on the upper ocean properties and are poorly known on the global scale. The relatively good agreement between simulated and observed global nutrient distributions shown in previous [e.g., *Six and Maier-Reimer*, 1996; *Schneider et al.*, 2008] and in this study (section 4) gives us confidence in our approach. Furthermore, *Six and Maier-Reimer* [1996] showed a good agreement even between simulated and observed seasonality for the surface ocean $pCO_2$ using this formulation of biological production.

[10] Phytoplankton growth $G_{phy}$ in HAMOCC depends on temperature, light, and nutrient availability following Michaelis-Menten kinetics. Light absorption is a function of water depth, and the local absorption coefficient includes clear water absorption for visible light and self-shading by phytoplankton [*Zielinski et al.*, 2002]. The growth rate is limited by the least available nutrient, i.e., nitrate, phosphate, or iron, with the half-saturation constants ($K_X$; Table 2) proportional to the used Redfield ratios.

$$\frac{\partial \text{Phy}}{\partial t} = G_{phy} - F_{pz} - M_{phy} - E_{phy},$$

$$G_{phy} = J(I,T) \frac{X}{K_X + X} \text{Phy} \quad \text{with}$$

$$X = \min\left(\text{PO}_4, \frac{\text{NO}_3}{R_{\text{N:P}}}, \frac{\text{Fe}}{R_{\text{Fe:P}}}\right), \qquad (2)$$

$$F_{pz} = \mu_{zoo} \frac{\text{Phy} - \text{Phy}_{min}}{K_{Zoo} + \text{Phy}} \text{Zoo},$$

$$M_{phy} = \lambda_{phy}(\text{Phy} - \text{Phy}_{min}),$$

$$E_{phy} = \beta_{phy}(\text{Phy} - \text{Phy}_{min}).$$

[11] Mortality of phytoplankton ($M_{phy}$) and exudation to DOM ($E_{phy}$) are calculated using mortality and exudation rates $\lambda_{phy}$ and $\beta_{phy}$, respectively. A minimum phytoplankton concentration (Phy$_{min}$) represents spores floating around to ensure potential phytoplankton

growth at any location. The growth rate ($J(I, T)$) depends on light $I(z)$ and temperature $T$ [see *Jassby and Platt*, 1976] following the light-saturation curve formulation by *Smith* [1936].

$$J(I,T) = \frac{g(I(z))f(T)}{\sqrt{g(I(z))^2 + f(T)^2}},$$

$$g(I(z)) = \alpha I_0$$

$$\left(\sigma \exp(-zk_r) + (1-\sigma)\exp\left(-zk_w - k_{chl}\int_0^z R_{\text{C:Chl}}\,\text{Phy}\right)\right),$$

$$f(T) = \mu_{phy}\,1.066^{(T)}. \qquad (3)$$

[12] $I_0$ is the daily-mean photosynthetically active fraction of incoming solar radiation at sea surface (PAR); $\alpha$ is the initial slope of the photosynthesis versus irradiance curve; $k_r$ and $k_w$ are mean absorption coefficients of seawater for the red and blue spectral domain of PAR (divided at about 580 nm as given by $\sigma$). Absorption coefficient for chlorophyll $k_{chl}$ is taken from observational data [*Zielinski et al.*, 2002]. The temperature dependency of growth $f(T)$ follows the Eppley curve [*Eppley*, 1972].

[13] Zooplankton grazing on phytoplankton ($F_{pz}$) is parameterized by a Monod equation with the half-saturation grazing constant ($K_{Zoo}$) and the maximum grazing rate ($\mu_{zoo}$). Grazing is limited by the minimum phytoplankton concentration that remains ungrazed. Only a part of the grazed bulk phytoplankton portion ($\omega_{zoo}\,\epsilon_{zoo}$) leads to zooplankton growth $G_{zoo}$, the remaining fraction is either egested as fecal pellets or recycled as dissolved nutrients. Natural senescence and carnivorous consumption of zooplankton ($M_{zoo}$) is represented by a quadratic formulation to slow down this consumption at low zooplankton concentrations. Similar to phytoplankton, this loss is restricted to a minimum concentration (Zoo$_{min}$) to ensure zooplankton existence at any location. For zooplankton, part of the carnivores activity leads to immediate release of dissolved nutrients and carbon, while the rest is considered as detritus (fecal pellets).

$$\frac{\partial \text{Zoo}}{\partial t} = G_{zoo} - M_{zoo} - E_{zoo},$$

$$G_{zoo} = \omega_{zoo}\,\epsilon_{zoo}\,F_{pz}, \qquad (4)$$

$$M_{zoo} = \lambda_{zoo}(\text{Zoo} - \text{Zoo}_{min})^2,$$

$$E_{zoo} = \beta_{zoo}(\text{Zoo} - \text{Zoo}_{min}).$$

[14] The production of DOM (considered as a semilabile form of DOM with a half lifetime of about 3 months) by zooplankton due to sloppy feeding and metabolic activities ($E_{zoo}$) is calculated with the rate $\beta_{zoo}$. It is remineralized with the rate $\lambda_{dom}$ as long as oxygen is available.

$$\frac{\partial \text{DOM}}{\partial t} = E_{phy} + E_{zoo} - \lambda_{dom}\,\text{DOM}. \qquad (5)$$

[15] Detritus is formed of dead cells of phytoplankton and zooplankton and of fecal pellets from zooplankton and carnivores activity.

$$\frac{\partial \text{Det}}{\partial t} = M_{\text{phy}} + (1 - \epsilon_{\text{zoo}})F_{\text{pz}} + (1 - \epsilon_{\text{can}})$$

$$M_{\text{zoo}} - \frac{\partial w_{\text{det}}\,\text{Det}}{\partial z} - F_{\text{det}},$$

with

$$F_{\text{det}} = (1 - \Gamma_{\text{O}_2})\lambda_{\text{det}}\,\text{Det} + \Gamma_{\text{O}_2}(\lambda_{\text{N}} + \lambda_{\text{S}} + \lambda_{\text{N}_2\text{O}})\text{Det}$$

$$\text{with} \quad \Gamma_{\text{O}_2} = \begin{cases} 1 & \text{if } \text{O}_2 < \text{O}_{2\text{crit}}, \\ 0 & \text{else}. \end{cases}$$

(6)

[16] Particles are exported out of the euphotic zone into the ocean interior with a constant settling velocity ($w_{\text{det}}$). Detritus is remineralized throughout the whole water column, depending on seawater oxygen concentrations (determined by a threshold value $\text{O}_{2\text{crit}} = 0.5$ $\mu$mol L$^{-1}$), either by aerobic remineralization with a constant rate $\lambda_{\text{det}}$ or by denitrification and sulphate reduction (within oxygen minimum zones) with rate constants $\lambda_{\text{N}}$, $\lambda_{\text{N}_2\text{O}}$, and $\lambda_{\text{S}}$, respectively.

[17] Macronutrients phosphate and nitrate as well as micronutrient dissolved iron are consumed by phytoplankton during photosynthesis and are released during detritus remineralization, zooplankton excretion, and bacterial degradation of DOM.

$$\frac{\partial \text{PO}_4}{\partial t} = -G_{\text{phy}} + \epsilon_{\text{zoo}}(1 - \omega_{\text{zoo}})F_{\text{pz}} + \epsilon_{\text{can}}M_{\text{zoo}}$$

$$+ \lambda_{\text{dom}}\,\text{DOM} + F_{\text{det}}.$$

(7)

[18] For nitrate, sources and sinks of biological processes are basically identical to equation (7). Only denitrification, where nitrate provides oxygen for remineralization in oxygen depleted zones, acts as an additional sink for nitrate ($D_{\text{NO}_3}$). At the air-sea interface atmospheric $\text{N}_2$ is fixed by bacteria such as cyanobacteria which adds nitrate to the system ($F_{\text{cyan}}$). Nitrogen fixation occurs only in areas where the ratio of nitrate to phosphate is lower than $R_{\text{N:P}}$. $R_{\text{denit}}$ is the ratio of mol nitrate consumed per mol phosphate in organic matter which is degraded by denitrifying bacteria. In a stationary ocean, denitrification and nitrogen fixation are balanced.

$$\frac{\partial \text{NO}_3}{\partial t} = \left(-G_{\text{phy}} + \epsilon_{\text{zoo}}(1 - \omega_{\text{zoo}})F_{\text{pz}} + \epsilon_{\text{can}}M_{\text{zoo}}\right.$$

$$\left. + \lambda_{\text{dom}}\,\text{DOM} + F_{\text{det}}\right)R_{\text{N:P}} - D_{\text{NO}_3} + F_{\text{cyan}},$$

with

$$D_{\text{NO}_3} = \Gamma_{\text{O}_2}R_{\text{denit}}\lambda_N\text{Det},$$

$$F_{\text{cyan}} = \mu_{\text{cyan}}(R_{\text{N:P}}\text{PO}_4 - \text{NO}_3) \quad \text{only} \quad \text{for NO}_3 < \text{PO}_4.$$

(8)

[19] Analogous to equation (7), transformations of dissolved iron are given by the equation below.

$$\frac{\partial \text{Fe}}{\partial t} = \left(-G_{\text{phy}} + \epsilon_{\text{zoo}}(1 - \omega_{\text{zoo}})F_{\text{pz}} + \epsilon_{\text{can}}M_{\text{zoo}}\right.$$

$$\left. + \lambda_{\text{dom}}\,\text{DOM} + F_{\text{det}}\right)R_{\text{Fe:P}} + F_{\text{air}} - F_{\text{lig}},$$

(9)

with

$$F_{\text{air}} = R_{\text{dust}} \text{ Dust only at sea surface and}$$

$$F_{\text{lig}} = \lambda_{\text{Fe}} \max(0, \text{Fe} - \text{Fe}_{\text{crit}}).$$

[20] For iron, there is an aeolian source ($F_{\text{air}}$) following the present-day dust deposition climatology (Dust; *Mahowald et al.* [2006]) and the assumption of a constant fraction of bioavailable iron content ($R_{\text{dust}}$). At dissolved iron concentrations larger than $\text{Fe}_{\text{crit}} = 0.6$ nmol L$^{-1}$, iron complexation by organic substances (ligands; $F_{\text{lig}}$) is assumed and dissolved iron is removed from the water column with a fixed rate ($\lambda_{\text{Fe}}$) [*Parekh et al.*, 2005; *Archer and Johnson*, 2000].

### 2.1.2. Marine Oxygen and Dinitrous Oxide Cycle

[21] Some biological processes, such as photosynthesis or remineralization also effect the oxygen concentration. Oxygen changes are related to changes in phosphate with a constant stoichiometric ratio $R_{\text{O}_2:\text{P}}$. Oxygen is produced during photosynthesis and is consumed during organic matter decay in an aerobic environment.

$$\frac{\partial \text{O}_2}{\partial t} = \left(G_{\text{phy}} - \epsilon_{\text{zoo}}(1 - \omega_{\text{zoo}})F_{\text{pz}} - \epsilon_{\text{can}}M_{\text{zoo}}\right.$$

$$\left. - \lambda_{\text{dom}}\,\text{DOM} - (1 - \Gamma_{\text{O}_2})\lambda_{\text{det}}\,\text{Det}\right)|R_{\text{O}_2:\text{P}}|.$$

(10)

[22] The aerobic remineralization of nitrogen in organic material occurs in a stepwise oxidation of its content to dissolved nitrate. The climate relevant gas dinitrous oxide ($\text{N}_2\text{O}$) is a side product of this nitrification. For simplification, the production of $\text{N}_2\text{O}$ is linked to the consumption of oxygen during remineralization of organic material.

$$\frac{\partial \text{N}_2\text{O}}{\partial t} = r_{\text{N}_2\text{O}}R_{\text{O}_2:\text{P}}\left(\epsilon_{\text{zoo}}(1 - \omega_{\text{zoo}})F_{\text{pz}} + \epsilon_{\text{can}}M_{\text{zoo}}\right.$$

$$\left. + \lambda_{\text{dom}}\,\text{DOM} + \lambda_{\text{det}}\,\text{Det}\right) - D_{\text{N}_2\text{O}}, \text{with}$$

$$D_{\text{N}_2\text{O}} = \Gamma_{\text{O}_2}(R_{\text{N}_2\text{O}}\lambda_{\text{N}_2\text{O}}\text{Det}).$$

(11)

[23] Following *Broecker and Peng* [1982], we assume that for every $10^4$ mol $\text{O}_2$ consumed one mol $\text{N}_2\text{O}$ is produced ($r_{\text{N}_2\text{O}}$). We neglect any aeolian deposition of $\text{N}_2\text{O}$. As we assume complete denitrification, i.e., nitrate and dinitrous oxide are reduced to dinitrogen, $R_{\text{N}_2\text{O}}$ denotes the ratio of mols $\text{N}_2\text{O}$ consumed to degraded 1 mol $\text{PO}_4$ of organic material.

### 2.1.3. Production of Planktonic Shell Material

[24] Aside from the production of organic material, most plankton species build skeleton structures from silicate or calcium carbonate ($\text{CaCO}_3$). Despite the single phytoplankton-type approach for primary production (see section 2.1.1), we separate two plankton fractions of detritus, as being opal- and calcium carbonate-producing, to reproduce observed distributions of silicate and alkalinity in the water column and the sediments. As indicated by well-documented plankton successions in blooms [e.g., *Lochte et al.*, 1993], opal-producing species (i.e., diatoms) show dominant abundance in the early blooming phases. Accordingly, we attributed the export flux of organic carbon to silicate

consumption: as long as silicate is available, opal production ($G_{opal}$) takes place. In silicate-depleted seawater, $CaCO_3$ production ($G_{CaCO_3}$) is assumed to be dominant. The good performance of this approach has been shown in previous studies [*Heinze et al.*, 2003; *Heinze*, 2004; *Ilyina et al.*, 2009; *Ilyina and Zeebe*, 2012]. Shell material is sinking with its distinct settling velocities ($w_{opal}$ and $w_{cal}$; different from that of detritus). Dissolution of opal is temperature dependent and is calculated with a rate coefficient ($\lambda_{opal}$) in the entire water column.

$$\frac{\partial Opal}{\partial t} = G_{opal} - \lambda_{opal} Opal - \frac{\partial w_{opal} Opal}{\partial z},$$
with
$$G_{opal} = R_{Si:P} \frac{Si}{K_{Si} + Si} \left( M_{phy} + (1 - \epsilon_{zoo}) F_{pz} \right.$$
$$\left. + (1 - \epsilon_{can}) M_{zoo} \right), \quad (12)$$

where $K_{Si}$ is the half-saturation constant for silicate uptake. Accordingly, changes in silicate are given by:

$$\frac{\partial Si}{\partial t} = -G_{opal} + \lambda_{opal} Opal. \quad (13)$$

[25] Dissolution of calcium carbonate ($D_{CaCO_3}$; note that only calcite is considered in the CMIP5 model version) is the product of the degree of undersaturation with respect to carbonate ion $[CO_3^{2-}]$, a dissolution rate constant ($\lambda_{cal}$), and the available solid material ($CaCO_3$).

$$\frac{\partial CaCO_3}{\partial t} = G_{CaCO_3} - D_{CaCO_3} - \frac{\partial w_{cal} CaCO_3}{\partial z},$$
with
$$G_{CaCO_3} = R_{Ca:P} \frac{K_{Si}}{K_{Si} + Si} \left( M_{phy} + (1 - \epsilon_{zoo}) F_{pz} \right.$$
$$\left. + (1 - \epsilon_{can}) M_{zoo} \right), \quad (14)$$

$$D_{CaCO_3} = \lambda_{cal} CaCO_3 \max \left( 0, \frac{S_{Ca}}{Ca^{2+}} - [CO_3^{2-}] \right), \quad (15)$$

where $S_{Ca}$ is the apparent solubility product of calcite and $Ca^{2+}$ is the calcium ion concentration (assumed to be constant at 10.3 mmol $kg^{-1}$).

### 2.1.4. Inorganic Carbon Chemistry

[26] Inorganic carbon chemistry in HAMOCC mainly follows *Maier-Reimer and Hasselmann* [1987] with a revised calculation of chemical constants (based on *Goyet and Poisson* [1989]). The two prognostic tracers considered in the model are total dissolved inorganic carbon ($TCO_2$) and total alkalinity (TA). $TCO_2$ is the sum of carbonic acid $[H_2CO_3]$, bicarbonate ion $[HCO_3^-]$, and carbonate ion $[CO_3^{2-}]$, i.e., $[TCO_2] = [H_2CO_3] + [HCO_3^-] + [CO_3^{2-}]$. TA in the model is the sum of carbonate and borate alkalinities, and water dissociation products, i.e., $[TA] = [HCO_3^-] + 2[CO_3^{2-}] + [B(OH)_4^-] + [OH^-] - [H^+]$.

[27] Carbonate species can be diagnostically determined by applying the classical mass action law for dissociation reaction, which is based on temperature, pressure, and salinity [e.g., *Goyet and Poisson*, 1989]. Similar to other state variables, $TCO_2$ and TA are transported with the 3-D flow field. Additionally, they are modified by several biogeochemical processes. Uptake of atmospheric $CO_2$ by seawater (section 2.2) increases $TCO_2$ without changing TA. The seasonal growth of phytoplankton results in a drawdown of $TCO_2$ and produces an increase in TA. Aerobic remineralization of organic matter has the reversed effect (section 2.1.1). TA and $TCO_2$ are consumed during planktonic production of $CaCO_3$ and released during its dissolution (section 2.1.3). Finally, TA changes occur in the processes of nitrogen fixation by algae and consumption of inorganic nitrogen during anaerobic remineralization (the reduction of $[NO_3^-]$ increases TA; see *Zeebe and Wolf-Gladrow* [2001] and section 2.1.1 for details). These processes are summarized in the two equations below.

$$\frac{\partial TCO_2}{\partial t} = R_{C:P} \left( -G_{phy} + \epsilon_{zoo} (1 - \omega_{zoo}) F_{pz} + \epsilon_{can} M_{zoo} \right.$$
$$\left. + \lambda_{dom} DOM + F_{det} \right) - G_{CaCO_3} + D_{CaCO_3}, \quad (16)$$

$$\frac{\partial TA}{\partial t} = -R_{N:P} \left( -G_{phy} + \epsilon_{zoo} (1 - \omega_{zoo}) F_{pz} + \epsilon_{can} M_{zoo} \right.$$
$$\left. + \lambda_{dom} DOM + F_{det} \right) + \Gamma_{O_2} (R_{denit} + R_{N_2O}) \lambda_n Det$$
$$- F_{cyan} - 2(G_{CaCO_3} + D_{CaCO_3}). \quad (17)$$

### 2.1.5. Marine Sulfur Cycle

[28] HAMOCC includes a simplified marine sulfur cycle described and evaluated in previous studies [*Kloster et al.*, 2006, 2007; *Six and Maier-Reimer*, 2006]. It comprises production, bacterial consumption, photolysis, and sea-air gas exchange of DMS. We restrict the sulfur cycle to DMS and do not include the precursor of DMS, dimethylsulfoniopropionate (DMSP), or oxidized compounds, such as dimethylsulfoxide (DMSO). In the ocean, DMSP is produced within the cells of marine phytoplankton for physiological functions such as osmolyte, antioxidant or cryoprotectant, but these are hitherto not fully understood. After a disruption of the plankton cell membrane by senescence or due to viral attack and zooplankton grazing intracellular DMSP is released into seawater and rapidly converted to DMS by enzyme systems of bacteria. It is known that the intracellular production of organic sulfur compounds varies between different species of phytoplankton. In general, phytoplankton-producing shells from $CaCO_3$ tend to have much higher sulfur to carbon cell ratios as opal building phytoplankton. Therefore, we relate DMS production to the production of shell material which itself is related to detritus production (see section 2.1.3). We include a temperature dependency, as intercellular

sulfur-to-carbon ratios of many species are higher in colder waters. Accordingly, a temperature dependency with $T_a = T + 3[^\circ C]$ allows for a slightly higher DMS production in cold water.

$$\frac{\partial \text{DMS}}{\partial t} = \left(1 + \frac{1}{T_a^2}\right)\left(\gamma_d G_{\text{opal}} + \gamma_c G_{\text{CaCO}_3}\right) \\ - \left(\gamma_{\text{photo}} \frac{g(I(z))}{\alpha} + \gamma_{\text{bac}} T_a \frac{\text{DMS}}{K_{\text{DMS}} + \text{DMS}}\right)\text{DMS}. \tag{18}$$

[29] Sulfur-to-carbon ratios in opal- and calcite-producing plankton are $\gamma_d$ and $\gamma_c$, respectively. The photolysis of DMS depends on the rate $\gamma_{\text{photo}}$ and the available solar radiation, as calculated in photosynthesis. There is no influx of DMS from the atmosphere (see section 2.2). Bacterial consumption is temperature dependent and follows Monod kinetics with a half-saturation constant $K_{\text{DMS}}$. The different values for $\gamma$ are taken from literature and adjusted within the observed range to achieve an optimal fit with observations [*Kloster et al.*, 2006].

## 2.2. Interactions With the Atmosphere

[30] Fluxes between the ocean and the atmosphere are computed for gaseous tracers such as $CO_2$, $O_2$, DMS, $N_2O$, and $N_2$ (Figure 1). Atmospheric concentrations of these tracers may be provided by the atmospheric model (e.g., for $CO_2$ in MPI-ESM), prescribed as being either time varying or assumed to be constant (e.g., for $O_2$), or set to zero (e.g., for DMS). Air-sea flux of a given gas $Y$ in the upper model layer is calculated as the deviation from the thermodynamic equilibrium given by the difference in concentrations across the air-sea interface ($Y^{\text{air}} - Y^{\text{sea}}$), multiplied by a kinetic parameter represented by the exchange rate for a given gas ($v_Y$) calculated using the temperature-dependent Schmidt number and piston velocity [*Wanninkhof*, 1992]. As this temperature dependency fit is only defined in the temperature range from 0 to about 30°C, calculated values for seawater concentrations at temperatures above 30°C (projected locally in the coming greenhouse world) may be biased (the fit gets negative above 42°C). Hence, HAMOCC 5.2 employs the revised temperature dependency of air-sea flux parameters for $CO_2$ and DMS following *Gröger and Mikolajewicz* [2011]. For $CO_2$, the partial pressure is calculated as the ratio between the actual seawater concentration and the solubility ($pCO_2 = CO_2/S_{CO_2}$); the values of $S_{CO_2}$ are given by *Weiss* [1974]. For $O_2$, the Schmidt number is computed according to *Keeling et al.* [1998], and the solubility is a function of temperature and salinity according to *Weiss* [1970]. The atmospheric partial pressure of $O_2$ is assumed constant and remains at the preindustrial level. While $O_2$ is consumed in the atmosphere during the combustion of fossil fuel, the resulting changes in atmospheric $O_2$ concentrations are assumed to be small and therefore neglected. For $N_2$ and $N_2O$, we apply the same piston velocity as for oxygen. The atmospheric $N_2$ concentration is set to a constant value. For $N_2O$ the corresponding atmospheric content is its seawater saturation value.

## 2.3. Sediment Biogeochemistry

[31] The sediment module in HAMOCC is described in *Heinze et al.* [1999] and essentially computes the same processes between dissolved tracers ($TCO_2$, TA, $PO_4$, $NO_3$, $O_2$, Fe, Si, and $N_2$) in pore water and solid sediment constituents (detritus, $CaCO_3$, opal, and terrigenous material) as in the water column (Figure 1). The sediment module has 12 biologically active layers and a diagenetically consolidated burial layer. The fraction between pore water and solid sediment is preset and fixed for each sediment layer. At the water-sediment interface pelagical sedimentation fluxes of detrital and shell material ($CaCO_3$ and opal) are added to the sediment and diffusive processes exchange dissolved compounds between pore water and the overlaying ocean water. Within the sediment, remineralization of organic material is described as in the water column: aerobic remineralization occurs as long as oxygen is available in pore water. At low oxygen levels ($\leq 0.5$ $\mu$mol L$^{-1}$), denitrification and sulfur reduction further reduces organic matter concentration. For opal and calcite we essentially apply the same dissolution processes as in the seawater (section 2.1.3): shell material is degraded depending on the degree of saturation and a constant dissolution rate. For opal we assume a silicate saturation concentration of 1 mmol Si L$^{-1}$ [*Heinze et al.*, 1999]. The carbonate concentration is calculated from pore water $TCO_2$ and TA, taking dissociation constants from the overlaying ocean water. Sediment accumulation, resulting from detrital and shell material deposition, might lead to a higher than prescribed fraction of solid constituents within a sediment layer. In this case, the sediment column is redistributed by shifting the surplus of solid compounds of the corresponding layer deeper into the sediment; thereby it can finally reach the burial layer.

## 3. Experimental Design

### 3.1. Implementation of HAMOCC Into MPIOM and MPI-ESM

[32] The model HAMOCC needs an ocean flow field to describe the transport and mixing of its tracers. Computation of advection and diffusion of biogeochemical parameters is the same as in an OGCM (MPIOM) for temperature and salinity. Effects of unresolved eddies in MPIOM are included into parameterizations of diffusive mixing of tracers along isopycnals, as well as in the vertical eddy viscosity and diffusion (details are given in *Jungclaus et al.* [2006] and references therein). In this way, the distribution of ocean biogeochemical and ocean circulation components is consistent. In the setup presented here, HAMOCC runs as a subroutine of MPIOM (Jungclaus et al., 2012, in press). The ocean model therefore determines HAMOCC's spatial and temporal resolutions (described in section 3.3). HAMOCC takes distributions of temperature and salinity from MPIOM to compute carbonate chemistry constants and transformation rates (section 2.1). The wind speed at 10 m height above sea level is used in the gas

exchange parameterization (section 2.2). Information on sea ice cover from MPIOM is used to modify light availability for phytoplankton growth and air-sea gas exchange. Technical details on the coupling of the two models are given in *Maier-Reimer et al.* [2005]. HAMOCC is conceptually designed for use with other OGCMs and has already been successfully implemented in other models (see section 1). The ocean and atmosphere components in MPI-ESM are coupled daily without flux corrections (Giorgetta et al., submitted manuscript, 2012).

## 3.2. CMIP5 Experiment Categories

[33] The general experimental design of CMIP5 simulations is given in *Taylor et al.* [2011]. In the following we discuss only those CMIP5 experiment categories that are evaluated and analyzed in this study. A summary of model scenarios is given in Table 3. In all CMIP5 simulations, MPIOM and HAMOCC are components of MPI-ESM (Giorgetta et al., submitted manuscript, 2012). Ocean biogeochemistry is addressed in two different types of simulations that serve different purposes:

[34] (a) Most CMIP5 simulations were performed with prescribed atmospheric $CO_2$ concentrations. These experiments are essential to evaluate the forced climate response and to compare the various CMIP5 models. The experiments of this type can be also used to diagnose a range of emissions of anthropogenic $CO_2$ which result in a projected warming in a given scenario. Also in all idealized experiments (referred to as 1% p.a. and abrupt $4 \times CO_2$; Table 3), the atmospheric $CO_2$ concentrations are prescribed.

[35] (b) A limited number of CMIP5 experiments have been performed with the fully coupled (interactive) carbon cycle and forced by greenhouse gas emissions.

[36] Simulations of category (a) with prescribed atmospheric $pCO_2$ were performed for the historical period (1850–2005), three future projections (RCP2.6, RCP4.5, and RCP8.5 as described in *Moss et al.* [2010]; not analyzed here) and idealized experiments (Table 3). Simulations of category (b) were performed for the historical period (esmHist) and only one future projection (RCP 8.5). In both setups, the carbon fluxes are diagnosed between the ocean and land reservoirs and the atmosphere respectively, but only in esmHist and

esmRCP8.5 they influence atmospheric concentrations of $CO_2$. These experiments include feedbacks between carbon cycle and climate as represented by MPI-ESM (section 5). The idealized experiments (esmFixclim and esmFdbk; Table 3) can be used to separate the effects of climate change and rising $CO_2$ concentrations on the uptake and storage of carbon in the ocean. In esmFixClim the atmospheric $pCO_2$ rises by 1% per year, but the radiation scheme is not influenced by this rise so that the climate remains at preindustrial level. In esmFdbk the same rise of atmospheric $pCO_2$ is prescribed, but the carbon cycle does not respond to ("see") this increase (section 6).

## 3.3. Geometry

[37] As a subroutine of the ocean model MPIOM, HAMOCC has the same spatial configuration. MPIOM uses either a bipolar grid with poles over Antarctica and Greenland, or a tripolar spherical coordinate system with two poles in the Northern Hemisphere located over Canada and Siberia (for details see Jungclaus et al., submitted manuscript, 2012). In current CMIP5 experiments, the model runs on both grid configurations: a relatively coarse bipolar grid referred to as MPI-ESM-LR (GR15; about 1.5° horizontal resolution) and a finer tripolar "eddy-permitting" grid MPI-ESM-MR (TP04; about 0.4° horizontal resolution). In the vertical direction, both LR and MR model configurations have 40 layers of varying thickness increasing in the bottomward direction. Horizontal resolution of the atmospheric model ECHAM6 (B. Stevens et al., The atmospheric component of the MPI Earth system model: ECHAM6, submitted to *Journal of Advances in Modeling Earth Systems*, 2012, hereinafter referred to as Stevens et al., submitted manuscript, 2012) is T63 (1.875°) for LR and MR configurations. In the vertical, ECHAM6 has 47 and 95 levels in LR and MR versions, respectively. Note that due to computational limitations, the LR model configuration was used for the majority of MPI-ESM CMIP5 experiments.

## 3.4. Initialization

[38] Originally, HAMOCC is initialized from globally uniform mean concentrations of ocean and pore water tracers. Such initialization requires a very long spin-up time (tens of thousands of years); it has been performed previously using a HAMOCC standalone version and

**Table 3.** Summary of CMIP5 Experiments (Following *Taylor et al.* [2011]) for Which Performance of the Model HAMOCC is Analyzed

| CMIP5 Experiment | Time Period | $CO_2$ Forcing |
|---|---|---|
| Control | 1850 + 500 yrs | Simulations with preindustrial $CO_2$ (and climate). |
| Hist | 1850–2005 | Historical concentrations of $CO_2$; simulations with prescribed atmospheric $CO_2$ concentrations. |
| esmHist | 1850–2005 | Historical emissions of $CO_2$; interactive carbon cycle. |
| Abrupt $4 \times CO_2$ | 1850 + 140 yrs | Instantaneous quadrupling of atmospheric $CO_2$ concentrations, kept constant thereafter. |
| 1% p.a. | 1850 + 140 yrs | Increase of atmospheric $pCO_2$ by 1% per year until $4 \times CO_2$. Both climate and carbon cycle respond to $CO_2$ forcing. |
| 1% p.a. esmFixClim | 1850 + 140 yrs | Same as 1% p.a. but only the carbon cycle responds to $CO_2$ forcing. |
| 1% p.a. esmFdbk | 1850 + 140 yrs | Same as 1% p.a. but only climate responds to $CO_2$ forcing. |

used to initialize the spin-up simulations of the MPIOM/HAMOCC. Within CMIP5, MPIOM/HAMOCC was spun-up for several thousands of years forced by climatological data sets and assuming a preindustrial atmospheric $CO_2$ concentration of 278 ppm. The resulting tracer fields were transferred into the MPI-ESM, and the spin up was continued in the coupled ocean-atmosphere mode for 1900 years (for details on the spin up procedure, see Jungclaus et al., submitted manuscript, 2012).

[39] During the initial phase of CMIP5 experiments, $CO_2$ fluxes in MPI-ESM were tuned to achieve consistency between land, atmosphere and ocean model components with respect to preindustrial atmospheric $CO_2$ concentrations. This was done with the purpose of reducing the spin-up time of model integrations. Throughout this process, weathering fluxes and $CaCO_3$ content in sediments have been increased, which led to elevation of TA (see section 4.2). This would have occurred naturally, without leading to excess TA, had the biogeochemistry model been given a long-enough spin-up time to equilibrate its sediments. However, along with this increase in TA also $TCO_2$ increased (with the molar ratio 2:1) so that the proportional over-estimation of this pair maintained the correct $pCO_2$. In an earlier study [*Ilyina et al.*, 2009], we showed that TA agreed well with observations in the HAMOCC stand-alone configuration in which the model was span up over several tens of thousands of years.

[40] All resulting distributions are evolving from the simulated physical and biogeochemical processes. There is no data restoring to observed values in HAMOCC and all chemical constituents (e.g., carbon, phosphorous, nitrogen or silica) are mass conserving within computational precision. This procedure makes the model particularly suitable for CMIP5 type of experiments where the future distribution of tracers is changing.

### 3.5. Forcing

[41] The main external forcing in the CMIP5 experiments is the rising atmospheric $pCO_2$, either from prescribed atmospheric values or from emissions (section 3.2). Additionally, external forcing for biogeochemical tracers in HAMOCC includes weathering fluxes and dust deposition. Riverine fluxes of carbon and nutrients are not considered in the CMIP5 suite of simulations (although a mechanism to include them exists in other HAMOCC versions). The aeolian iron forcing is fixed in all CMIP5 experiments (section 2.1.1).

[42] Despite a relatively long spin-up run of MPI-ESM (section 3.4), the time constants related to sedimentary processes are so large that a quasi-stationary equilibrium of the solid sediment constituents in the burial layer is not yet achieved [*Heinze et al.*, 1999; *Archer et al.*, 1993]. Especially with regard to $CaCO_3$, the remaining permanent small flux of carbonate affects the alkalinity and, thus, the oceanic carbon cycle. To account for the carbonate and silicate loss of the water column, we analyzed the fluxes into the sediment over the last 300 years of the spin-up runs and prescribed a globally uniform weathering input for silicate, alkalinity, and dissolved inorganic carbon (Table 4). Note that even small differences in ocean circulation in various model configurations affect sediment fluxes. Hence, they had to be diagnosed separately in MR and LR models. In the MR configuration, for instance, there was a flux of silicate out of the sediment (indicating that the model was not yet in a fully stationary state) so that the weathering flux of silicate was set to zero.

## 4. Evaluation of Present-Day Model Results

[43] In the following, we evaluate the biogeochemistry model performance in the experiment Hist (Table 3) against observations (listed in section 4.1). First, we compare horizontal distributions of modeled present day ocean $pCO_2$, $TCO_2$, TA, oxygen, nitrate, phosphate, and silicate at the sea surface and also at 100, 500, 1000, and 3000 m (except for $pCO_2$) computed in the LR and MR model configurations with observations (Figures 2–12). Additionally, globally integrated values of biogeochemical parameters are summarized in Table 4 to aid in evaluating model performance. To better show the improvement of model results in the higher resolution experiment (MR), we subtract the absolute difference between the model and observations in the MR runs from that of the LR runs (i.e., the differences between abs(Model$_{LR}$ − Obs) and abs(Model$_{MR}$ − Obs) in the bottom portion in Figures 2–8). Any improvement of model results with respect to observations due to the resolution increase will show up as regions of positive values. We also evaluate the model using Taylor diagrams [*Taylor*, 2001] in Figure 15 and quantitative statistical metrics as suggested by *Allen et al.* [2007],

**Table 4.** Globally Integrated Values of Biogeochemical Parameters Calculated in the Model HAMOCC in Different Experiments and Spatial Resolutions for the Year 1850

|  | Units | Hist LR | Hist MR | esmHist LR |
|---|---|---|---|---|
| Primary production | GtC yr$^{-1}$ | 61.58 | 55.83 | 61.63 |
| $CaCO_3$ production | GtC yr$^{-1}$ | 0.90 | 0.87 | 0.92 |
| Opal production | Tmol Si yr$^{-1}$ | 127.64 | 103.09 | 125.36 |
| Export production at 90 m | GtC yr$^{-1}$ | 9.07 | 8.23 | 9.07 |
| $N_2$ fixation | Tmol N yr$^{-1}$ | 14.89 | 11.25 | 15.48 |
| Denitrification | Tmol N yr$^{-1}$ | 14.53 | 12.13 | 14.77 |
| Weathering rates for $CaCO_3$ | Tmol C yr$^{-1}$ | 28.42 | 31.58 | 28.42 |
| Weathering rates for Si | Tmol Si yr$^{-1}$ | 6.32 |  | 6.32 |
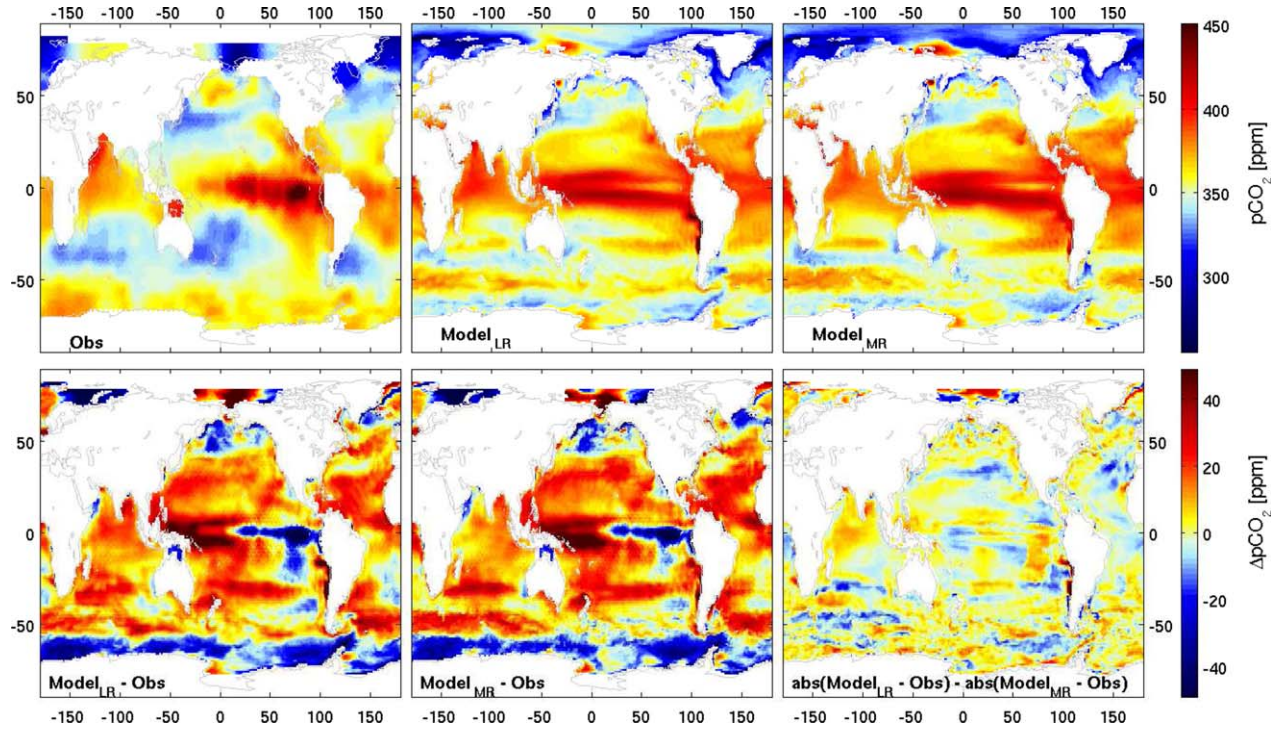
**Figure 2.** Comparison between model and observations for seawater $pCO_2$ (ppm): Upper left portion shows climatological annual mean $pCO_2$ from *Takahashi et al.* [2009]; upper middle and left portions from the historical runs in LR and MR model configurations, respectively. Lower left and middle portions show differences between model and observations for LR and MR configurations; and the right portion shows the differences of differences so that values $> 0$ indicate an improvement toward the MR model configuration.
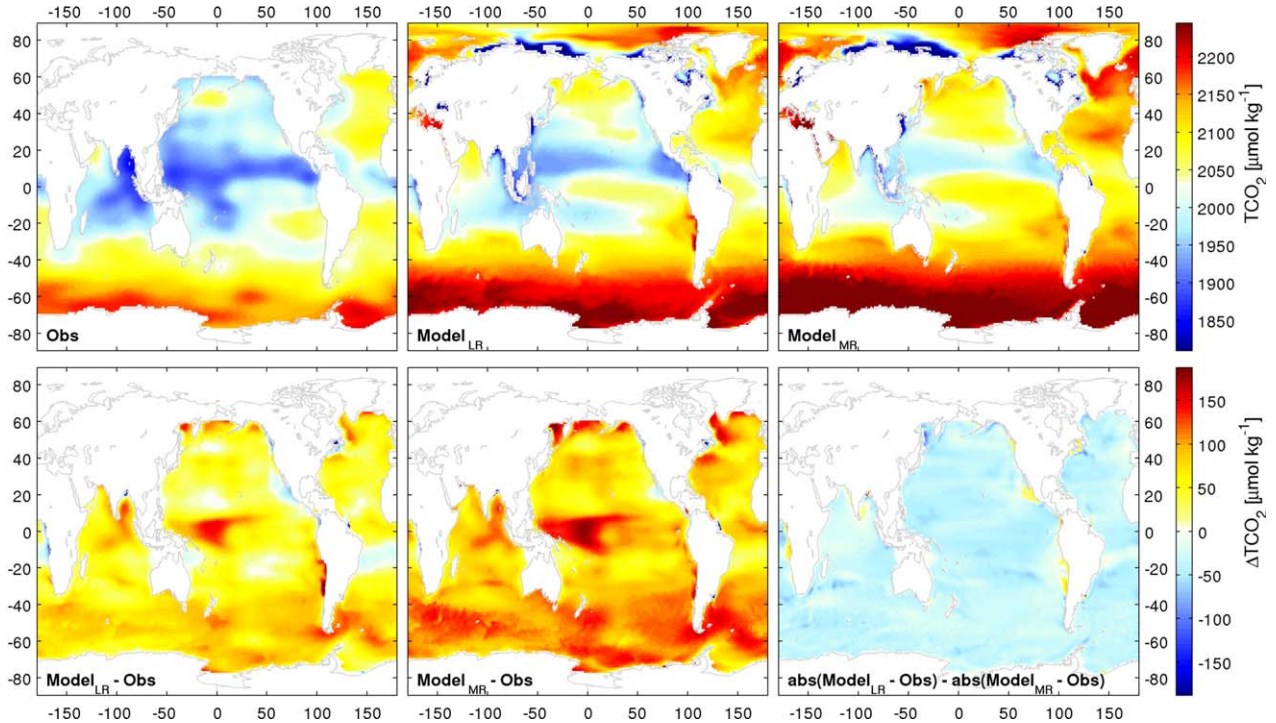


**Figure 3.** Same as Figure 2 but for surface $TCO_2$. Observations are annual mean fields from the GLODAP database.
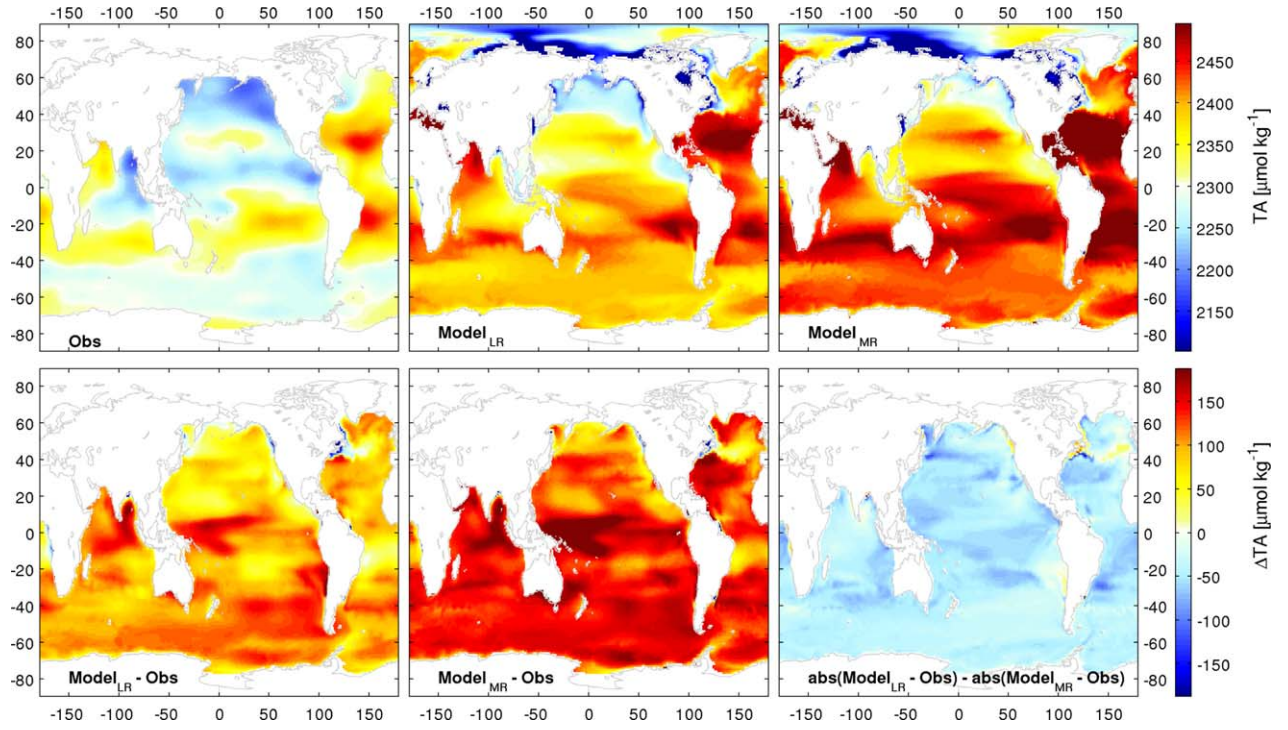
**Figure 4.** Same as Figure 2 but for surface TA. Observations are annual mean fields from the GLODAP database.
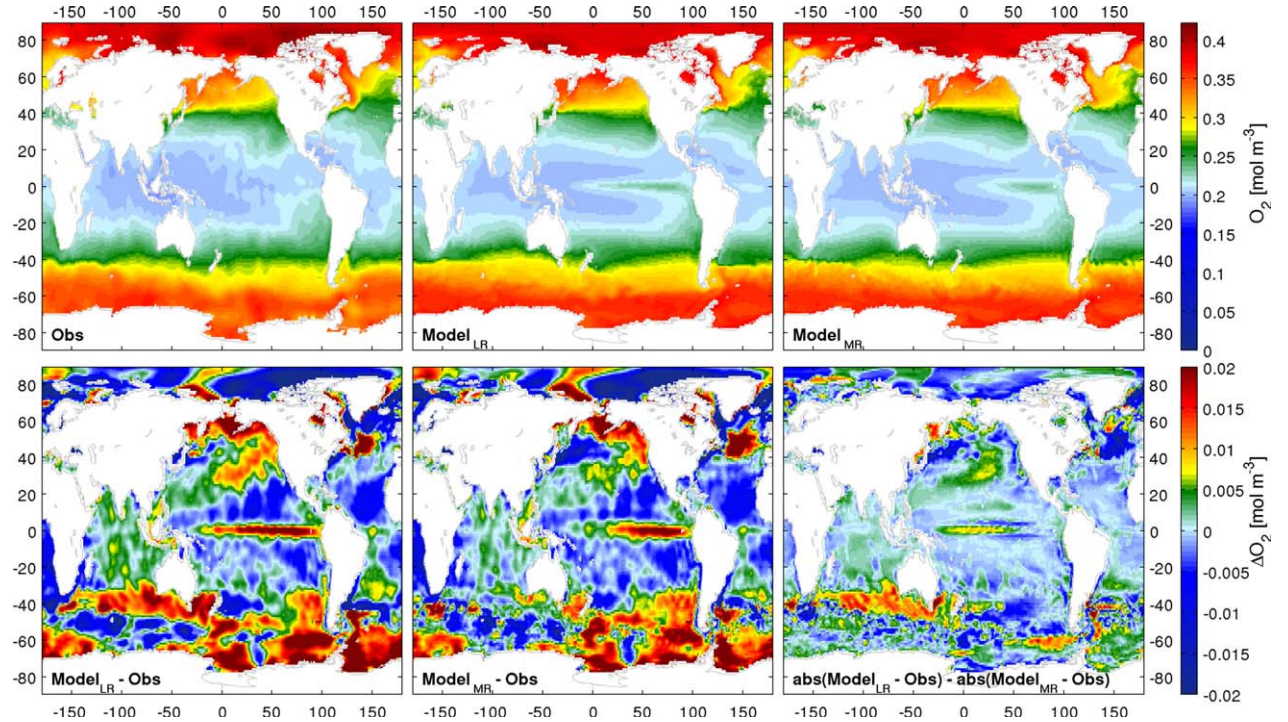


**Figure 5.** Same as Figure 2 but for surface oxygen. Observations are annual mean fields from WOA.
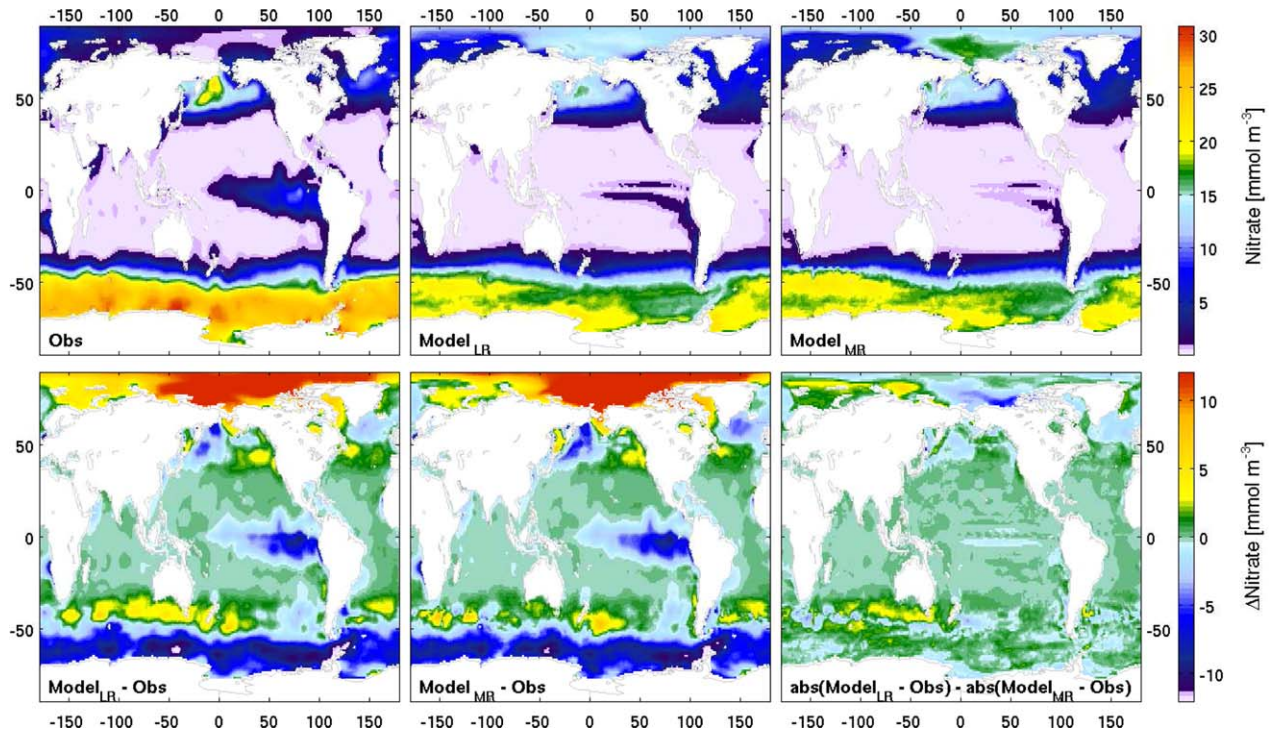
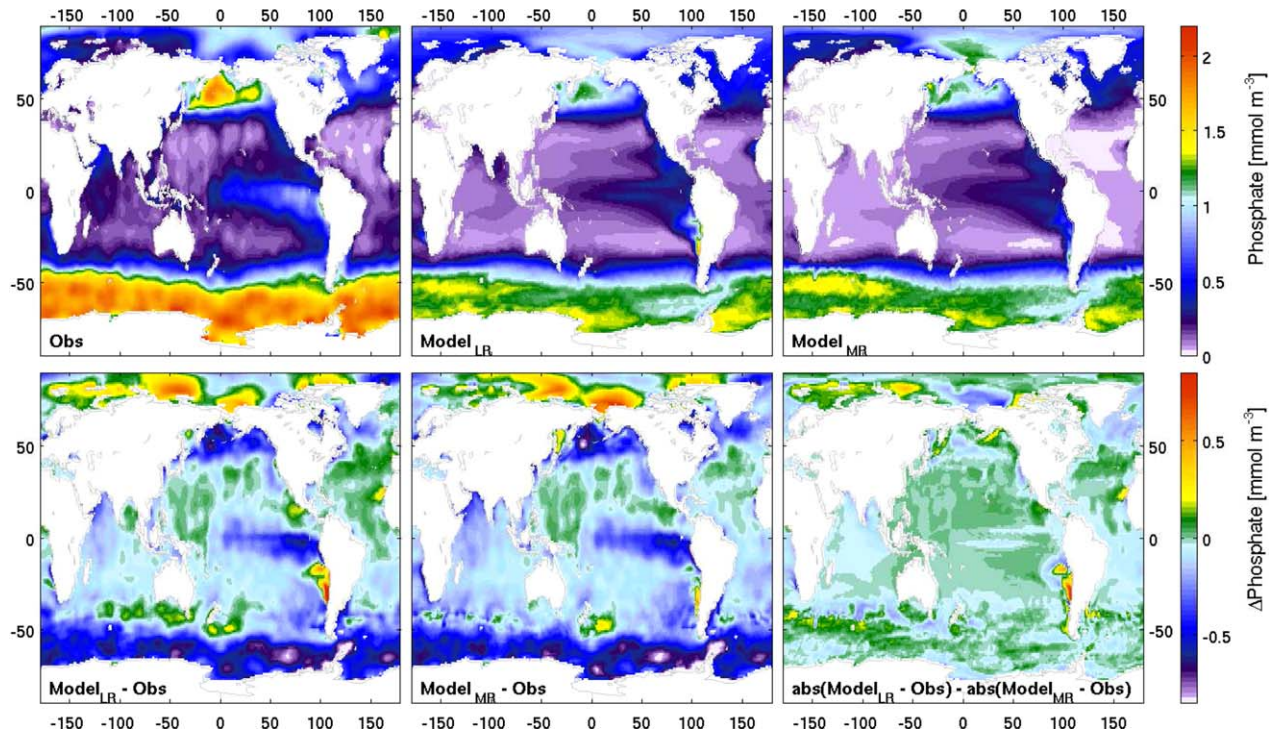**Figure 6.** Same as Figure 2 but for surface nitrate. Observations are annual mean fields from WOA.



**Figure 7.** Same as Figure 2 but for surface phosphate. Observations are annual mean fields from WOA.
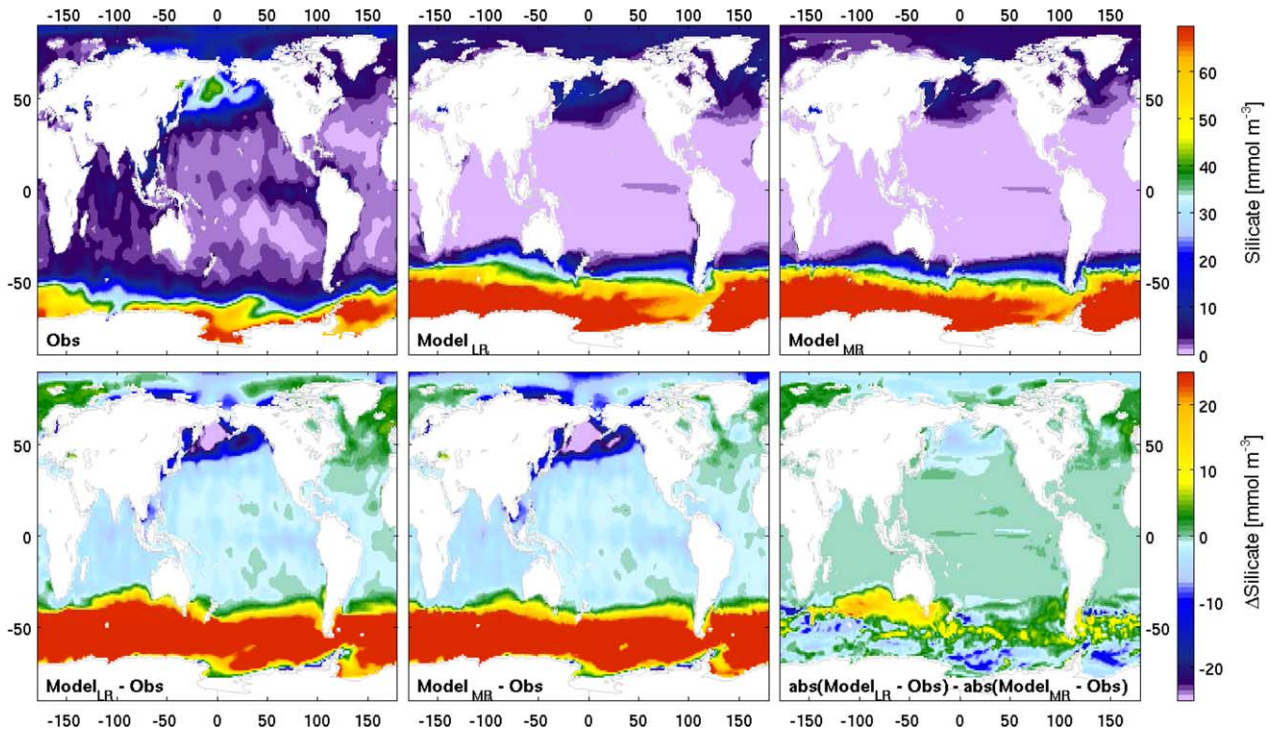
**Figure 8.** Same as Figure 2 but for surface silicate. Observations are annual mean fields from WOA.

*Stow et al.* [2009], and *Bhattacharyya* [1943] (summarized in Table 5).

### 4.1. Observational Basis

[44] We employed several observational databases for the evaluation of model results: A climatological mean distribution of the surface ocean $pCO_2$ compiled by *Takahashi et al.* [2009] was used to assess the model performance with respect to spatial patterns of $pCO_2$. Three dimensional distributions of ocean carbonate chemistry (TA and $TCO_2$) gridded onto $1° × 1°$ are available through the Global Data Analysis Project (GLODAP; *Key et al.* [2004]). Data from the World ocean atlas (WOA) [*Locarnini et al.*, 2010; *Garcia et al.*, 2010a, 2010b] was used to evaluate modeled distributions of phosphate, silicate, nitrate, and oxygen.

### 4.2. Comparison Between Modeled and Observed Spatial Distributions of Biogeochemical Variables

[45] Modeled $pCO_2$ is averaged over the years 1999 and 2001, which yields a slightly better match with observations than comparing to the year 2000 only (the reference year in *Takahashi et al.* [2009]). Other ocean biogeochemical tracers are averaged over the time periods corresponding to observations (spanning the years 1972–1990 for $TCO_2$ and TA; 1950–2008 for nitrate; 1933–2008 for phosphate and silicate; and 1921–2008 for oxygen). Note that the historical CMIP5 experiments ran only until the year 2005, limiting the averaging time period accordingly. Due to the sparse observational database for iron, we don't compare its modeled and observed distributions.

[46] Spatial distribution of the annual mean $pCO_2$ is in fairly good agreement with observations (Figure 2) given the limitations of both model formulations and the compilation of observations. The simulated annual global flux of $CO_2$ into the ocean is roughly 2 Pg C $yr^{-1}$ in the 1990s (see section 5), being in agreement with observation based estimates of *Takahashi et al.* [2009]. The model overestimates the spatial extent of high $pCO_2$ values in the equatorial Pacific Ocean. The atmospheric model is known to overestimate convection over the Pacific warm pool and hence, trade winds are too strong (Stevens et al., submitted manuscript, 2012), resulting in a too strong upwelling at the eastern ocean boundaries in the model. This appears to be a common phenomenon in most state-of-the-art ESMs [*Roy et al.*, 2011]. The model also underestimates surface ocean $pCO_2$ in the Southern Ocean as a result of the inability of the ocean model to produce the correct water mass property in the Antarctic Circumpolar Current (ACC) system. Largest positive biases in SST are also produced in the Southern Ocean and in the North Atlantic (with values below 1 degree; see Jungclaus et al., submitted manuscript, 2012, for details). Additionally, uncertainties in the parameterization of sea ice (D. Notz et al., The sea ice model in the MPI-ESM, submitted to *Journal of Advances in Modeling Earth Systems*, 2012, hereinafter referred to as Notz et al., 2012, in press), particularly due to accumulation and release of the respiratory $CO_2$ from under the sea ice [*Takahashi et al.*, 2002], might contribute to the Southern Ocean $pCO_2$ bias in the biogeochemical model. There is no visible improvement with resolution, i.e., in the eddy-permitting MR model
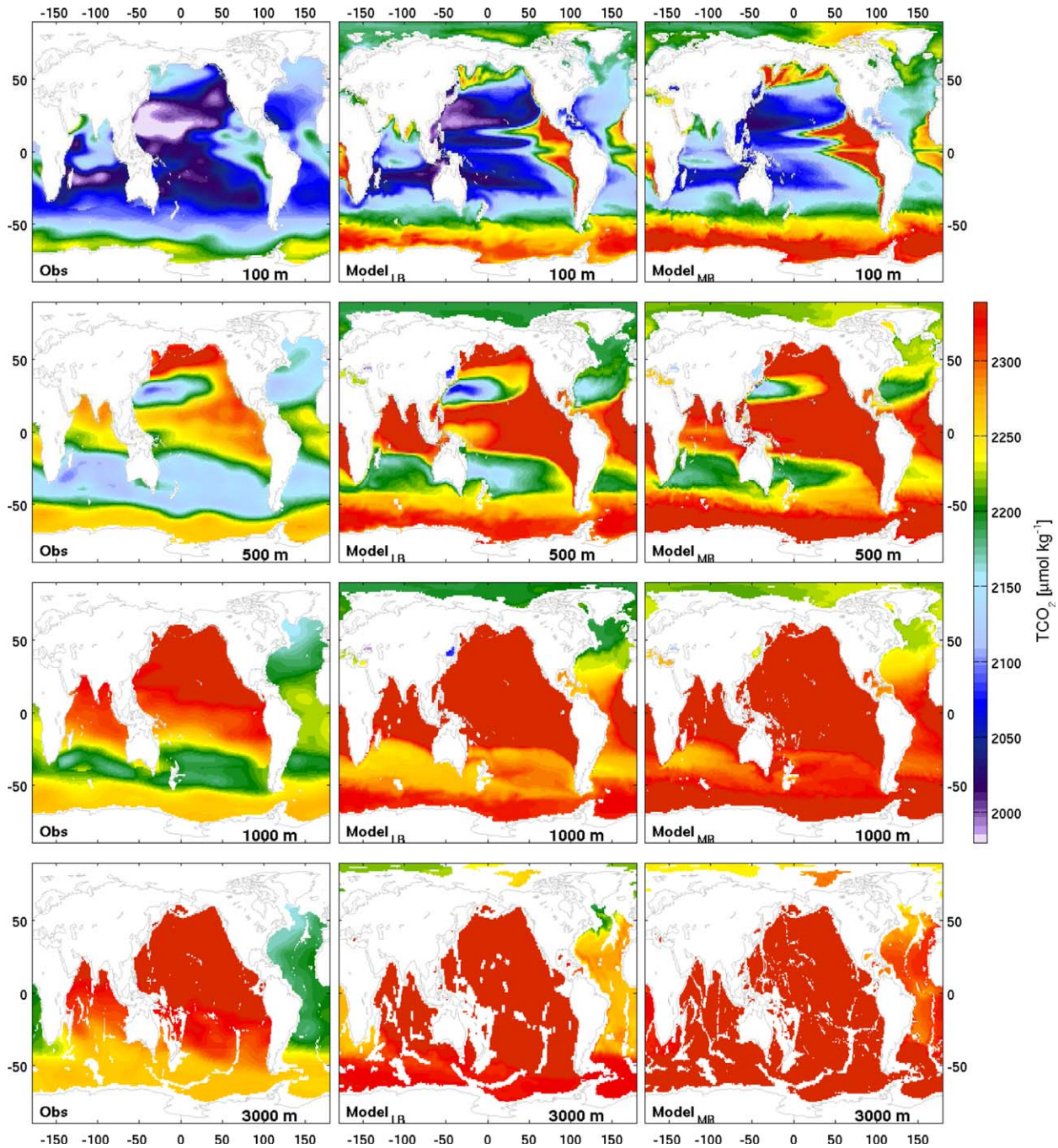
**Figure 9.** $TCO_2$ at different depth horizons. Observations are annual mean fields from the GLODAP database.

compared to its lower resolution counterpart (see discussion in the following sections). Likewise, only minor improvements in the model capability to reproduce SST are attributed to the MR configuration (Jungclaus et al., submitted manuscript, 2012).

[47] The model also captures the spatial patterns of the observed surface $TCO_2$ and TA (Figures 3 and 4), reproducing higher values in the subtropical gyres (similar to surface salinity distribution patterns) and, for $TCO_2$ also in the Southern Ocean. The absolute values of both $TCO_2$ and TA are overestimated in the CMIP5 experiments. Since TA affects the capacity of the ocean to take

up and store atmospheric $CO_2$, it was tuned during the spin up simulation to achieve a consistent representation of the oceanic $CO_2$ sink within MPI-ESM (section 3.5). Changes in TA are accompanied by changes in $TCO_2$ so that an overestimation in the TA and $TCO_2$ pair maintains a correct $pCO_2$ field. Largest overestimations in TA and $TCO_2$ are produced in the western equatorial Pacific. The overestimation of $TCO_2$ and TA persists throughout the water column and increases with depth (Figures 9 and 10), reaching 200 $\mu$mol kg$^{-1}$ at a depth of 3000 m.

[48] Modeled oxygen at the ocean surface (Figure 5) reflects temperature distribution and captures the cold
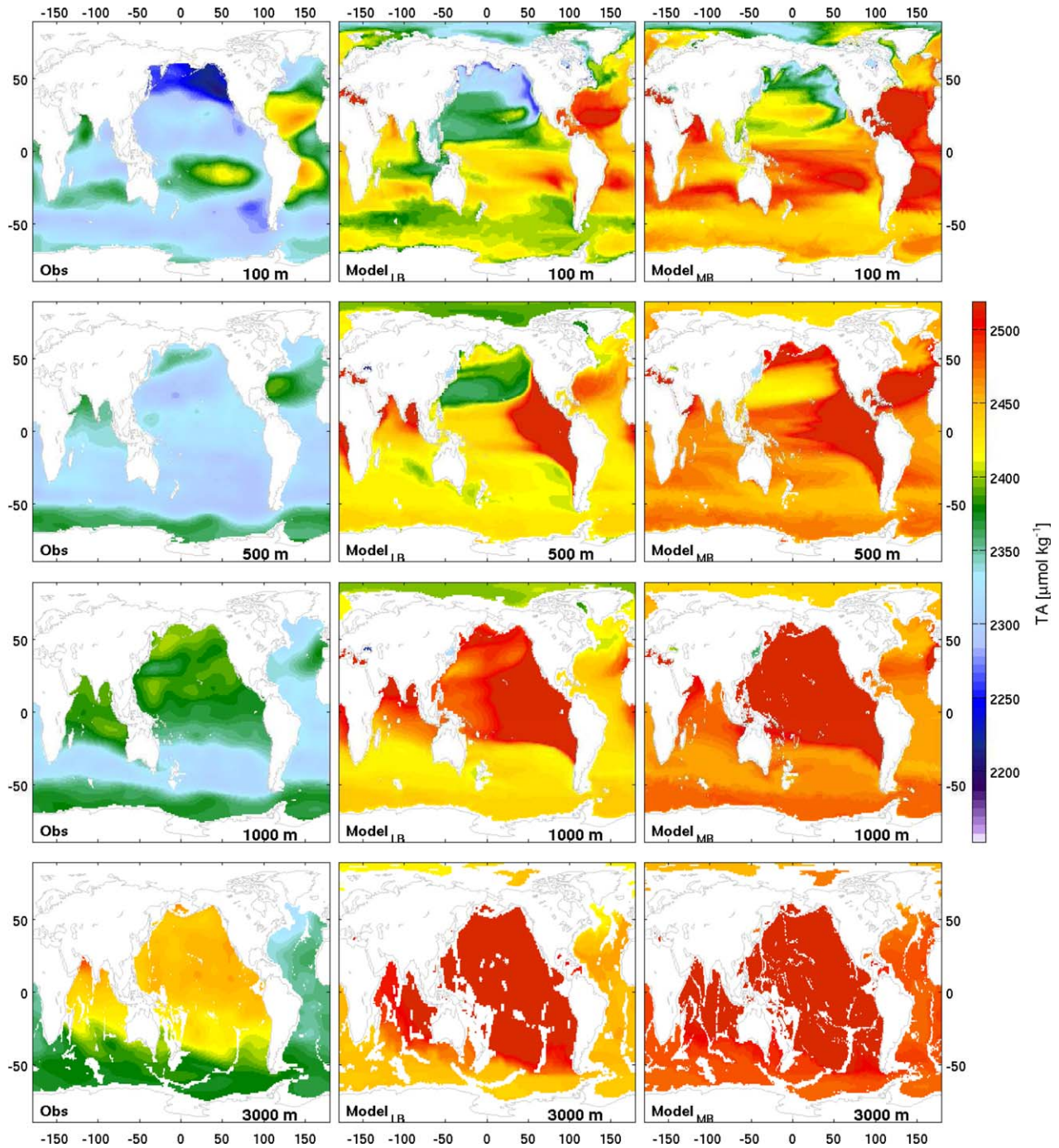
**Figure 10.** Same as Figure 9 but for TA. Observations are annual mean fields from the GLODAP database.

and oxygen-rich areas in the Arctic and the Southern Ocean and warmer and lower oxygen concentration areas elsewhere. This indicates that the solubility effects determine the distribution of oxygen at the ocean surface. In the deeper model layers (Figure 11), the prominent oxygen minimum zones (OMZ) in the eastern equatorial Pacific and in the eastern tropical Atlantic (EEP and ETA, respectively), as well as in the Arabian Sea and the Bay of Bengal are reproduced. The model overestimates the size of the OMZ in the EEP and off

the coast of Namibia and produces lower than observed oxygen concentrations in these areas (see Figure 11 at 500 m). Such pattern is common in the global ocean biogeochemistry models, owing to their coarse resolution and simple globally tuned parameterizations of vertical fluxes of organic matter [*Cocco et al.*, 2012; *Andrews et al.*, 2012]. Low oxygen areas spread along the eastern Pacific coasts of both Americas in the model at 1000 m, occupying areas larger than observed. On the contrary, the model produces higher than observed
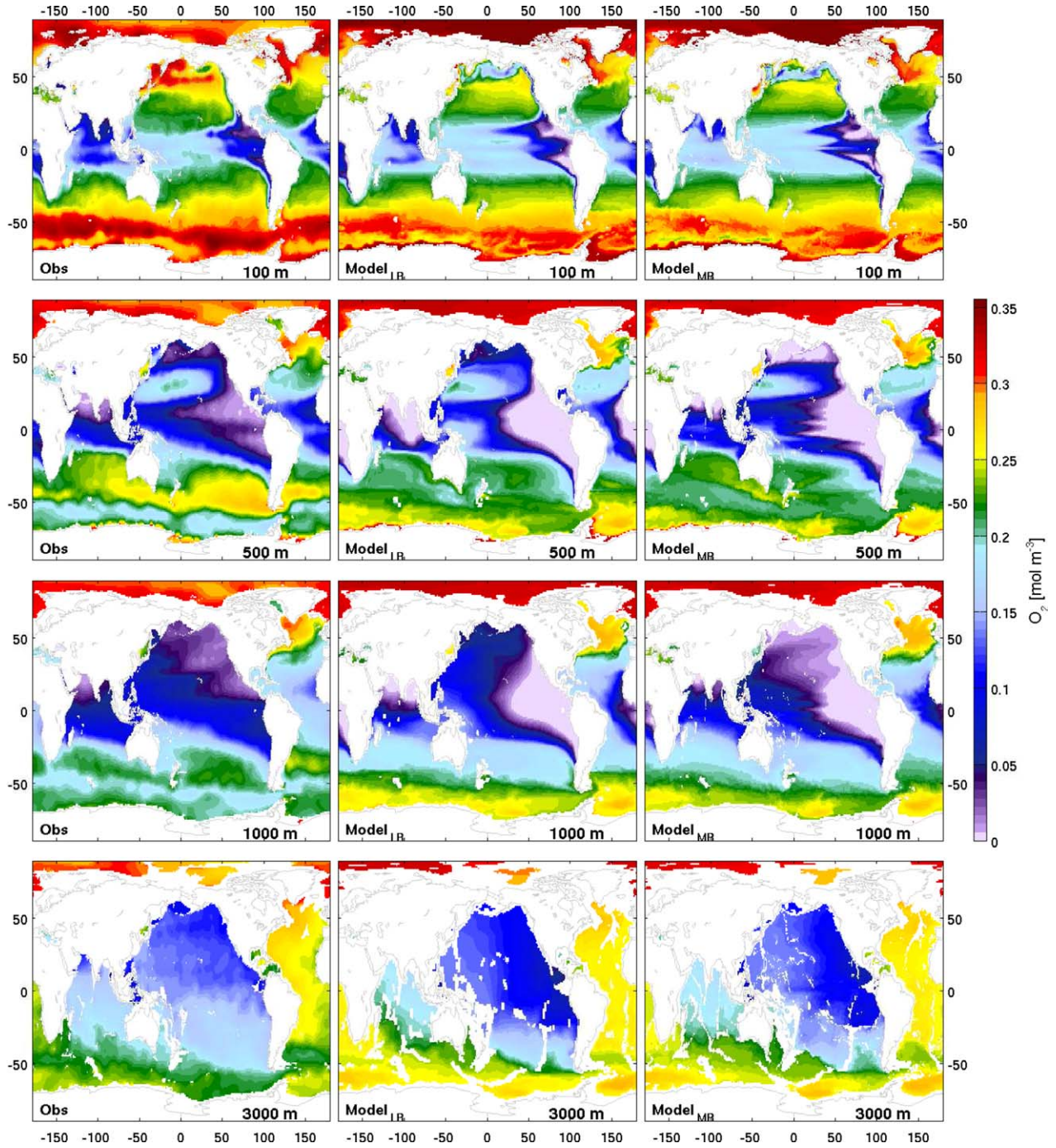
**Figure 11.** Same as Figure 9 but for oxygen. Observations are annual mean fields from WOA.

oxygen concentrations in the ACC system and in the Arctic Ocean due to intensive ventilation of these ocean areas (Jungclaus et al., submitted manuscript, 2012). Below the thermocline, i.e., at 3000 m (Figure 11; lower portion), modeled and observed values match quite well in the Pacific and Atlantic Ocean basins; the model overestimates oxygen concentrations in the Southern Ocean. According to visual analysis of Figure 11, the MR model configuration seems to better capture the details of the spatial patterns than the LR model at all depths. This is however not confirmed by quantitative metrics (see Table 5 and discussion in section 4.3).

[49] The concentrations of nitrate are slightly under-estimated in the model in the Southern Ocean both at the surface (Figure 6) and at depths (Figure 12). They are overestimated in the surface Arctic Ocean. The model produces lower than observed nitrate concentrations in the EEP and ETA, and in the northern Indian Ocean (Figure 12; at 500 m). This is consistent with the overestimated size of the OMZs in the model (see
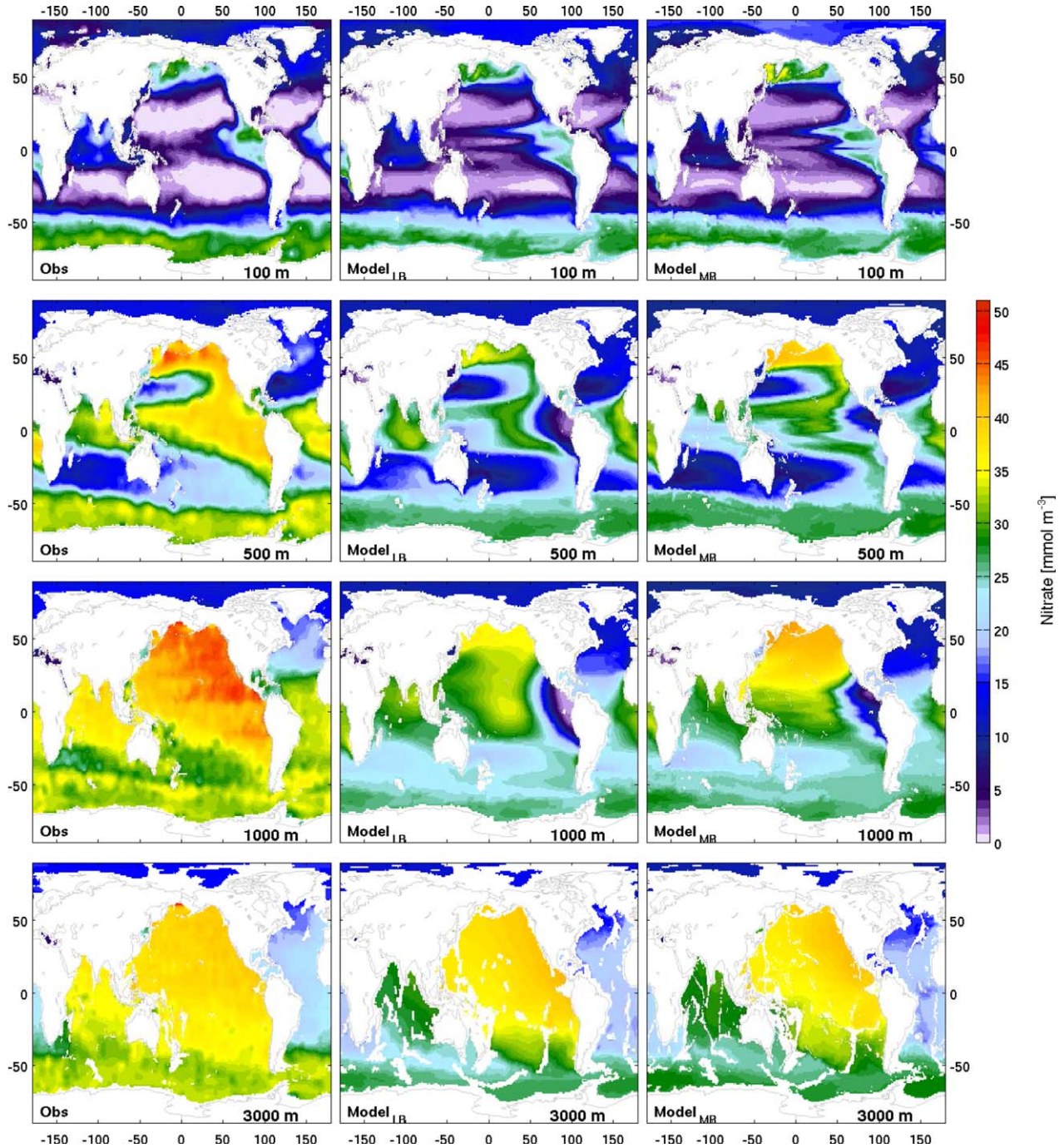
303

**Figure 12.** Same as Figure 9 but for nitrate. Observations are annual mean fields from WOA.

above) and indicates too strong denitrification in the model which occurs in oxygen depleted areas. Consequently, too low nitrate concentrations are spread throughout the water column, more pronounced in the LR than in the MR model configuration. Moreover, the formulation of nitrogen fixation is rather simple in this model version (cf. section 2.1). $N_2$ fixation simulated in the model (Table 4) is consistent with the observed abundances of nitrogen-fixing organisms (e.g., compiled in *Monteiro et al.* [2010]) in the tropics, the North Atlantic Ocean and in the Arabian Sea. A too strong $N_2$ fixation is present in the EEP where the model produces an upwelling of water strongly depleted in nitrate versus phosphate.

[50] High phosphate values at the surface in the Southern Ocean and phosphate-depleted areas in the subtropical Pacific, Atlantic, and the Indian Ocean (Figure 7) are reproduced in model results. Similar to nitrate, the model tends to underestimate surface phosphate in the ACC and in the North Pacific, likely due to

**Table 5.** Metrical Comparison of MPI-ESM-LR and -MR Outputs With Observations

| Depth | Variable | Correlation Coefficient (R) | | Ratio of Standard Deviations (RSD) | | Model Efficiency (ME) | | Percentage Model Bias (MB) | | Root-Mean-Square Error (RMSE) | | Bhattacharyya Distance (BD) | |
|---|---|---|---|---|---|---|---|---|---|---|---|---|---|
| | | LR | MR | LR | MR | LR | MR | LR | MR | LR | MR | LR | MR |
| Surface | $pCO_2$ | 0.66 | 0.68 | 1.09 | 1.14 | 0.11 | 0.10 | 2.13 | 2.27 | 0.06 | 0.06 | 0.02 | 0.16 |
| | $TCO_2$ | 0.92 | 0.93 | 1.09 | 1.09 | 0.61 | 0.01 | 1.72 | 3.34 | 0.02 | 0.04 | 0.33 | 0.36 |
| | TA | 0.79 | 0.79 | 1.21 | 1.26 | −0.09 | −2.11 | 1.50 | 3.28 | 0.02 | 0.04 | 0.84 | 0.69 |
| | Oxygen | 0.99 | 0.99 | 1.02 | 1.02 | 0.97 | 0.98 | 0.66 | 0.26 | 0.04 | 0.04 | 0.11 | 0.09 |
| | Nitrate | 0.87 | 0.87 | 0.78 | 0.80 | 0.75 | 0.74 | −2.62 | −2.97 | 0.66 | 0.68 | 0.04 | 0.04 |
| | Phosphate | 0.95 | 0.94 | 0.75 | 0.77 | 0.78 | 0.76 | −23.31 | −27.17 | 0.41 | 0.43 | 0.04 | 0.05 |
| | Silicate | 0.79 | 0.81 | 1.71 | 1.78 | −0.45 | −0.45 | 70.89 | 62.01 | 1.85 | 1.85 | 0.17 | 0.14 |
| 100m | $TCO_2$ | 0.89 | 0.89 | 1.31 | 1.34 | 0.17 | −0.82 | 2.01 | 3.60 | 0.03 | 0.04 | 0.17 | 0.09 |
| | TA | 0.86 | 0.89 | 1.08 | 1.12 | −0.20 | −3.34 | 1.60 | 3.41 | 0.02 | 0.04 | 0.11 | 0.12 |
| | Oxygen | 0.91 | 0.89 | 1.11 | 1.06 | 0.77 | 0.76 | −1.77 | −2.08 | 0.13 | 0.14 | 0.07 | 0.08 |
| | Nitrate | 0.93 | 0.92 | 0.89 | 0.94 | 0.85 | 0.84 | 8.46 | 8.07 | 0.33 | 0.35 | 0.09 | 0.08 |
| | Phosphate | 0.91 | 0.92 | 0.90 | 0.94 | 0.83 | 0.83 | −5.10 | −8.33 | 0.29 | 0.29 | 0.08 | 0.04 |
| | Silicate | 0.79 | 0.81 | 1.45 | 1.52 | 0.05 | 0.05 | 48.46 | 40.59 | 1.30 | 1.30 | 0.09 | 0.05 |
| 500m | $TCO_2$ | 0.64 | 0.76 | 2.43 | 1.97 | −4.23 | −3.10 | 3.25 | 4.04 | 0.06 | 0.06 | 0.17 | 0.15 |
| | TA | 0.15 | 0.25 | 2.88 | 2.19 | −18.81 | −28.39 | 3.10 | 4.55 | 0.04 | 0.05 | 0.21 | 0.28 |
| | Oxygen | 0.92 | 0.93 | 1.14 | 1.11 | 0.79 | 0.84 | −1.43 | −3.79 | 0.21 | 0.19 | 0.10 | 0.08 |
| | Nitrate | 0.74 | 0.89 | 0.77 | 0.88 | 0.12 | 0.42 | −22.99 | −21.54 | 0.33 | 0.27 | 0.05 | 0.18 |
| | Phosphate | 0.76 | 0.87 | 1.48 | 1.29 | 0.05 | 0.47 | −4.92 | −12.04 | 0.37 | 0.28 | 0.11 | 0.12 |
| | Silicate | 0.83 | 0.86 | 0.92 | 0.97 | 0.65 | 0.71 | 17.26 | 6.48 | 0.53 | 0.48 | 0.22 | 0.18 |
| 1000m | $TCO_2$ | 0.66 | 0.76 | 2.97 | 2.69 | −7.04 | −6.45 | 3.75 | 4.67 | 0.07 | 0.07 | 0.32 | 0.24 |
| | TA | 0.46 | 0.52 | 3.21 | 3.08 | −17.31 | −26.80 | 3.34 | 4.79 | 0.05 | 0.06 | 0.32 | 0.37 |
| | Oxygen | 0.92 | 0.95 | 1.21 | 1.22 | 0.75 | 0.82 | 0.88 | −2.08 | 0.24 | 0.21 | 0.23 | 0.16 |
| | Nitrate | 0.73 | 0.82 | 0.80 | 0.94 | −0.43 | −0.12 | −27.24 | −24.65 | 0.33 | 0.29 | 0.05 | 0.35 |
| | Phosphate | 0.76 | 0.83 | 1.74 | 1.61 | −0.41 | −0.02 | −4.78 | −9.67 | 0.36 | 0.31 | 0.40 | 0.29 |
| | Silicate | 0.90 | 0.90 | 0.93 | 0.88 | 0.79 | 0.82 | 9.89 | 2.83 | 0.29 | 0.27 | 0.15 | 0.14 |
| 3000m | $TCO_2$ | 0.94 | 0.94 | 1.62 | 1.42 | −0.31 | −1.09 | 2.11 | 3.30 | 0.03 | 0.04 | 0.17 | 0.43 |
| | TA | 0.92 | 0.92 | 1.74 | 1.47 | −2.60 | −5.08 | 2.43 | 3.47 | 0.03 | 0.04 | 0.32 | 0.24 |
| | Oxygen | 0.95 | 0.95 | 1.36 | 1.26 | 0.72 | 0.80 | 2.93 | 3.18 | 0.14 | 0.12 | 0.13 | 0.10 |
| | Nitrate | 0.92 | 0.95 | 1.13 | 1.10 | 0.56 | 0.63 | −11.54 | −11.40 | 0.15 | 0.14 | 0.40 | 0.36 |
| | Phosphate | 0.91 | 0.93 | 1.15 | 1.13 | 0.53 | 0.56 | −11.49 | −12.44 | 0.16 | 0.16 | 0.25 | 0.38 |
| | Silicate | 0.87 | 0.91 | 1.66 | 1.34 | −1.04 | −0.03 | 47.18 | 35.96 | 0.62 | 0.45 | 0.17 | 0.18 |

too low iron limitation. Phosphate is overestimated at the surface in the Arctic Ocean and at depth in the EEP (Figure 13). Note that during denitrification nitrate is consumed and phosphate is remineralized. This explains the mismatch in distributions between the two nutrients in the EEP. There is a tendency for improvements in the surface phosphate concentrations in the higher resolution model configuration (Table 5): the model-observations mismatch is slightly less in the MR runs compared to the LR, especially in the Southern and the Arctic Oceans (positive values in the bottom right portion in Figure 7).

[51] Unlike the concentrations of the nutrients phosphate and nitrate, silicate is overestimated in the ACC system (Figure 8). This overestimation slightly decreases with depth (Figure 14). Lower than observed concentrations are modeled at the surface over the vast areas of the tropical and subtropical ocean. Similar to phosphate, also silicate concentrations are overestimated in the EEP at 1000 m depth. At 3000 m the model computes higher than observed silicate concentrations, especially in the Pacific Ocean basin. Geographical distributions of silicate also indicate the commonly observed gross patterns of the opal export production [*Heinze et al.*, 2003, 1999]: high production

rates are located in the areas of high vertical velocities (and thus elevated vertical supply of silicic acid to the surface ocean) such as in the tropical upwelling zones and in the Southern Ocean. Accordingly, little amount of opal is produced in the large oligotrophic mid latitudinal gyres.

### 4.3. Model Skill Assessment Based on Quantitative Statistical Metrics

[52] We use statistical metrics following *Allen et al.* [2007] and *Stow et al.* [2009] to evaluate the skill of HAMOCC 5.2 to reproduce the observations (summarized in Table 5). These metrics allow us to determine which variables are better represented in the model and, eventually, to compare the model's performance with that of other models. Beside the metrics suggested by *Allen et al.* [2007] and *Stow et al.* [2009], we also include a measure of the similarity between the probability density functions of observations and model output, i.e., the Bhattacharyya distance (BD); *Bhattacharyya* [1943]. This allows comparing the similarity of patterns in model and observations even if they do not have the same geographical distribution, e.g., if minima and maxima are not located at the same positions.
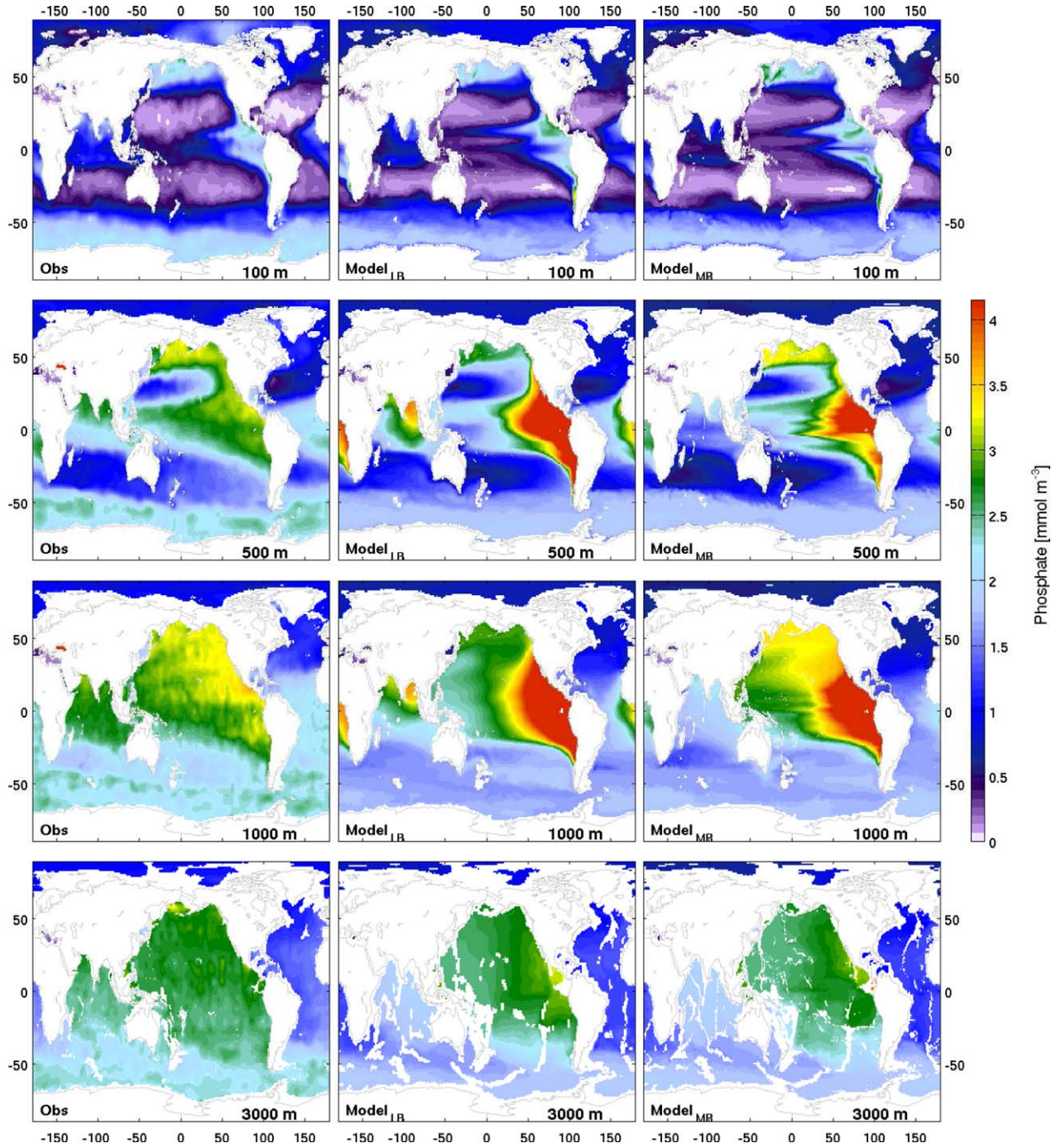
**Figure 13.** Same as Figure 9 but for phosphate. Observations are annual mean fields from WOA.

[53] The correlation coefficient ($R$) indicates the correlation between observations and model taken geographically one to one: If a variable changes from position $(i,j)$ to position $(i,j+1)$ in the same way in model and observations, $R$ is close to 1, suggesting that the model reproduces well the variable's spatial distribution (valleys and hills in a 3-D plot look similar in model and observations, though they can have different amplitudes). Note that $R$ close to 1 indicates that the changes from a point to the neighboring one in model and observations are similar (both increase or both decrease), but $R$ does not indicate the magnitude of the spatial variations (the height of the valleys and hills in a 3-D plot). Because of this, the ratio of standard deviations (RSD) between model and observations is used. An RSD close to one indicates that the model has a spatial variability similar in magnitude to the observations' one. Note also that $R$ provides no information on how
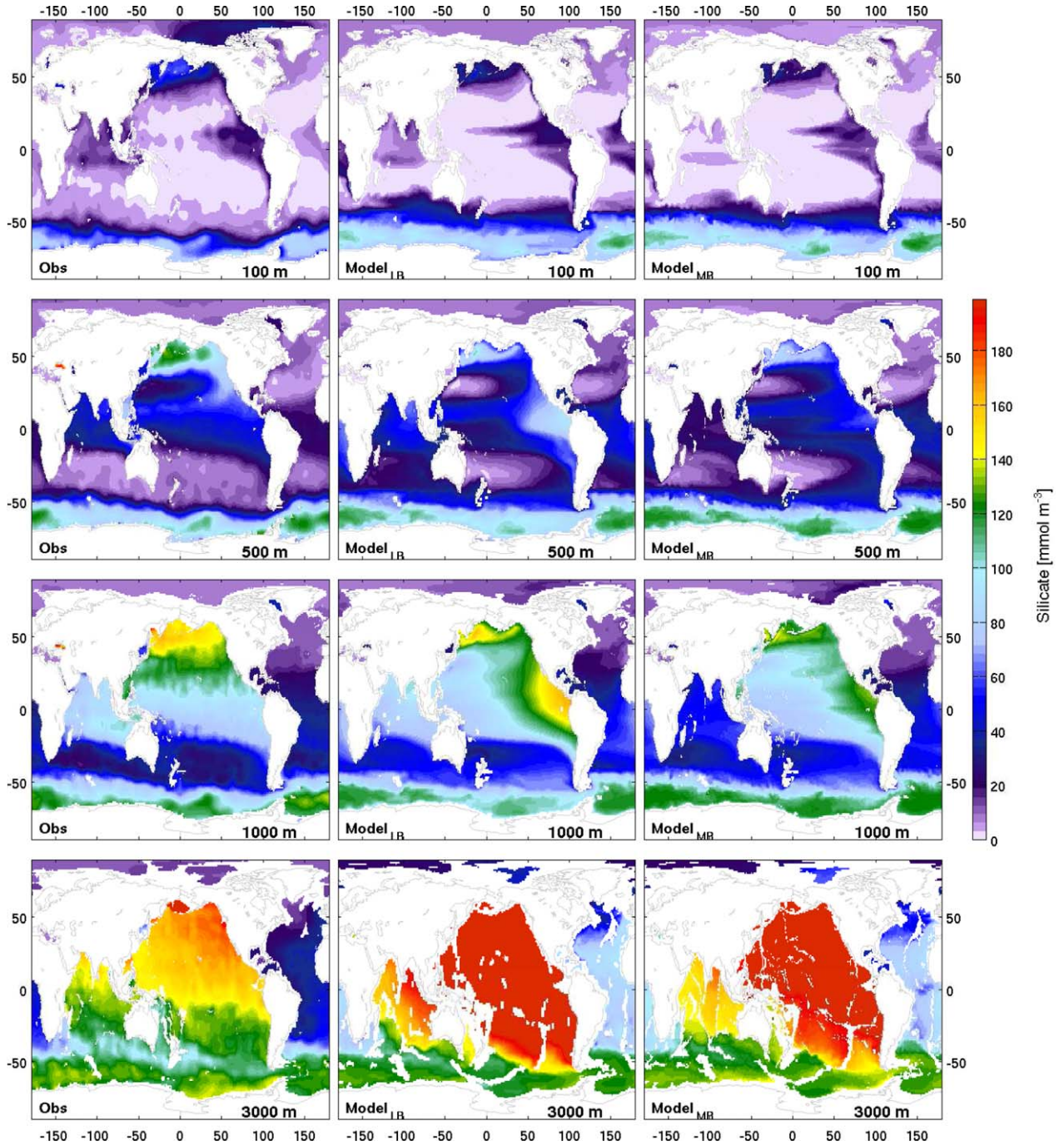
**Figure 14.** Same as Figure 9 but for silicate. Observations are annual mean fields from WOA.

good the model reproduces the mean state of the variable. For this the model efficiency (ME) and also the percentage model bias (MB) are used. One expects from a model to be able of reproducing observations in the range of natural variability of the corresponding process. Hence, the ME is defined as 1 minus the ratio between model error and observed variability. If the deviation between model and observations is larger than the observed variability, the ME is close to zero or is negative. Therefore, values less than 0.2 are catego-

rized as poor [*Allen et al.*, 2007; *Maréchal et al.*, 2004] and the model is "perfect" if ME equals 1. MB indicates whether the model is systematically underestimating or overestimating the observations. MB is calculated as the ratio of the sum of deviations of model and observations relative to the sum of the observations on a percentage basis. Small absolute values of MB (less than 40; *Maréchal et al.* [2004]) indicate a good performance of the model. Root-mean-square error (RMSE) is a measure of the general deviation of the model from the
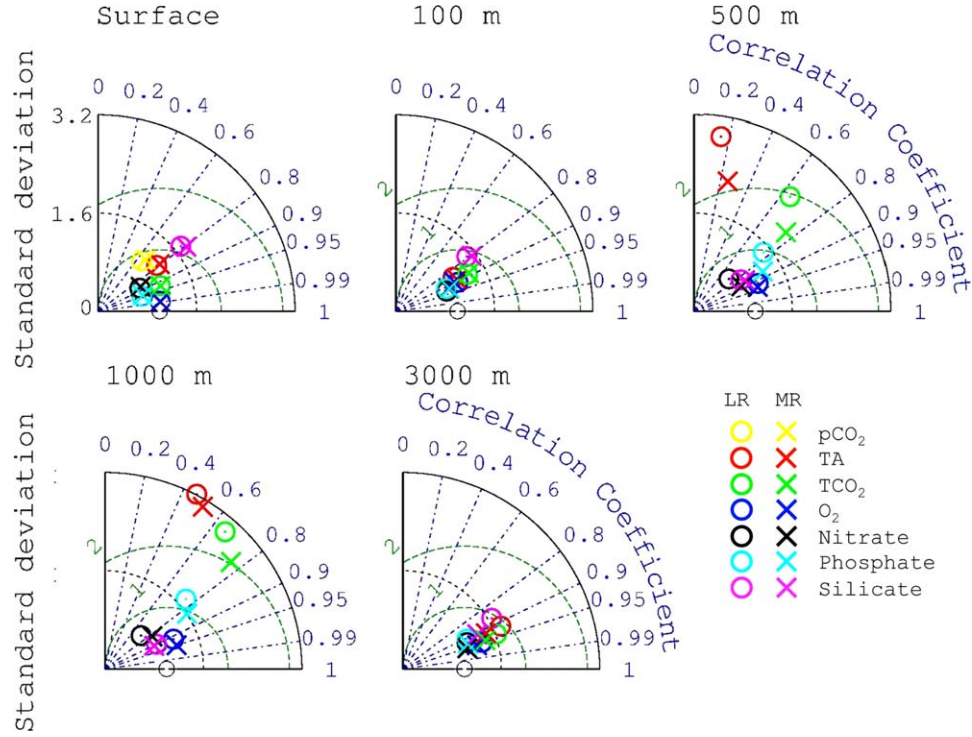
**Figure 15.** Taylor diagrams of several key ocean biogeochemistry diagnostics (represented by different colors) in CMIP5 experiments. Observational database is given in section 4.1. Modeled values are from the historical MPI-ESM-LR (shown by circles) and MPI-ESM-MR (shown by crosses) experiments.

observations, or a model bias with the small value considered as "good," and a large value as "bad," thereby complementing the ME and MB. The Bhattacharyya distance (BD) is a measure of the similarity between the probability density functions (pdfs) of observations and model output, where the pdfs are obtained from sampling the observations and model results at equidistant intervals for a common data range.

[54] We first estimate the model performance with respect to the ocean surface values: $R$ (Table 5) and RSD of almost all properties are close to 1, indicating that the model reproduces well the observed spatial distributions. The largest deviations here correspond to $pCO_2$ ($R = 0.66$, i.e., indicating deficiencies in the representation of the spatial distribution) and silicate (RSD = 1.71, i.e., lacking representation of the spatial variance). $R$ for phosphate is 0.95, considerably better than the correlation of about 0.8 for the four models tested by *Schneider et al.* [2008]. ME is less than 0.2 for $pCO_2$, TA, and silicate, indicating that the model error is larger than the observational spatial variability for half of the tested variables. MB indicates an overestimation of silicate and underestimation of phosphate (confirmed by the visual analysis of Figures 7 and 8 with the strongest differences in the Southern Ocean). While $pCO_2$ has a poor R and ME in comparison to other variables, its BD is the smallest one, suggesting a good representation of the observed pattern.

[55] Quantitative metrics for depth levels 100, 500, 1000, and 3000 m (Table 5) indicate that 21 of 36 metrics at the 100 m depth improve in comparison to the

surface, suggesting a general better representation of observations at this depth. The levels deeper than 100 m show generally a larger deviation of the model results from observations. The deepest level (3000 m) performs better than the 500 and 1000 m depth levels, particularly with regard to $R$. This indicates better representation of the spatial distribution of the variables closer to the ocean bottom. This improvement could be due to topographic constraints and homogenization of the variables. The horizontal area where the variables can spread reduces a lot at 3000 m depth and the variables are more homogeneously distributed or mixed at depth in the absence of major sources and sinks, presenting less structure or spatial variability than at the surface. Metric analysis also allows comparing the match of simulated variables with observations at the various depth levels: variables better represented at 100 m depth than at the surface are TA, nitrate, phosphate, and silicate, while at the deeper levels only silicate is better represented than at the surface.

### 4.4. Sensitivity of Model Performance to Different Spatial Resolutions

[56] We compare the two spatial model resolutions (LR and MR) using quantitative metrics in Table 5. At the ocean surface, there is little to no improvement in the representation of model parameters in the finer resolved model configuration. This is a consequence of the same horizontal resolution of the atmospheric model and the same coupling frequency between ocean and atmosphere in LR and MR configurations. A little

improvement in silicate is achieved in the MR version. The MR model, however, improves considerably in the deeper levels compared to the surface in comparison to LR. At 100 m depth and below most model variables (except for TA) perform better in MR than in LR configuration. Also Taylor diagrams (Figure 15) for various variables at the surface, 100 m, 500 m, 1000 m, and 3000 m depth, for LR (circles) and MR (crosses) confirm this conclusion. In a Taylor diagram, the observations are represented by a standard deviation and correlation of 1. Any deviations from 1 for either standard deviation or correlation represent a mismatch of modeled variables from observations. The larger the deviation, the worse is the model performance. Comparison of the circles and crosses indicates that while the performance at the surface is almost identical, the model bias in MR is smaller than in LR at depth. This is particularly true for intermediate depths (500 and 1000 m), where the crosses are clearly closer to 1 than the circles. Furthermore, Taylor diagrams also show that most model variables (for instance $TCO_2$, TA, oxygen, and nitrate) perform better at the surface or below 3000 m than at intermediate depths for both resolutions. These findings are in agreement with those of *Schneider et al.* [2008] and are confirmed by other statistical metrics (Table 5). Also indicated by the Taylor diagrams and the metrical analysis is that one of the better represented variables at the surface is $O_2$. While silicate seems to be the only variable that improves at intermediate depths it shows somewhat worse performance at the surface (with $R = 0.8$ and RMS=1 at the surface and $R = 0.9$ and RMS=0.5 at 1000 m depth).

[57] The influence of the resolution change on the model capability to represent spatial patterns can be demonstrated if we subtract the absolute difference of the model and observations in the MR runs from the LR runs (Figures 2–8). This identifies the regions with a better match with observations due to the resolution change. Changes in $pCO_2$ with resolution are patchy, and a concluding remark is difficult. However, there seems to be a general improvement in the tropics and southern subtropics, consistent with the improvements in the MR version of MPIOM (Jungclaus et al., submitted manuscript, 2012). MR seems to be counterproductive in the northern Atlantic and the northern Pacific. Note, however, that we are comparing a bipolar and a tripolar grid with no homogeneous grid size, which means that there are regions, e.g., around Greenland which actually have a slightly higher resolution in the LR (bipolar grid) than in the MR (tripolar grid) model version (Jungclaus et al., submitted manuscript, 2012). Distinct improvements in surface concentrations of oxygen (Figure 5), nitrate (Figure 6), phosphate (Figure 7), and silicate (Figure 8) in the MR resolution are in the ACC system (especially in its Indian Ocean sector), indicating a potential significance of eddies in this region. Analogous to statistical metrics, visual analysis also indicates that the MR improves the match with observations at depth rather than at the surface, particularly at 500 m and below and mostly for the eastern boundary in the tropical Pacific and Atlantic Oceans.

Note that the improvement at depth is due to horizontal (and not vertical) resolution. The improvement of the model at depth in the eastern boundary regions is also confirmed by comparing data and observations at vertical transects at 5°E and 85°W (not shown). This could indicate a better representation of coastal Ekman pumping (and therefore of upwelling) at the equator in the MR model configuration.

## 5. Internal Model Variability in the Simulations With Prescribed and Interactive Atmospheric $CO_2$

[58] Comparison of simulations with and without climate change performed within the Coupled Climate Carbon Cycle Model Intercomparison Project (C4MIP) [*Friedlingstein et al.*, 2006] demonstrated that the ocean and land carbon sinks noticeably decrease under global warming due to climate-carbon cycle feedbacks. Positive feedbacks between climate change and the carbon cycle lead to a higher airborne fraction of anthropogenic $CO_2$ emissions, and therefore to an acceleration of global warming [*Cox and Jones*, 2008]. Hence, simulations with the interactive carbon cycle belong to the set of standard experiments within CMIP5. Different sets of experiments with an interactive (free) carbon cycle have already been performed with the MPI-ESM precursor Earth system model COSMOS revealing a good reproduction of historical data [*Roeckner et al.*, 2011] and a stable interactive carbon cycle over the last millennium (Junglcaus et al., 2010). This model has also been used to study responses of the global carbon cycle (Brovkin et al., 2010) and ocean biogeochemistry (Segschneider et al., 2013) to large-scale volcanic eruptions. Here we discuss MPI-ESM CMIP5 simulations for the historical period (1850–2005) forced by (see details in section 3.2) prescribed atmospheric $pCO_2$ and by anthropogenic emissions of $CO_2$, referred to as experiments Hist and esmHist, respectively (Table 3). Only in experiment esmHist fluxes of carbon between ocean and atmosphere and between land reservoirs and atmosphere have a direct impact on the atmospheric $CO_2$ concentration and, hence, on climate. Note that simulations with interactive atmospheric $CO_2$ concentrations were performed only in LR model configuration.

[59] As a result of different forcing, atmospheric $CO_2$ concentration is not a globally uniform value in experiment esmHist. The near-surface (1000 hPa) atmospheric $CO_2$ concentrations in esmHist are higher than in Hist, especially over the continental regions of the Northern Hemisphere where the main sources of anthropogenic $CO_2$ emissions are located. The largest differences in atmospheric near surface $pCO_2$ over the ocean are found in the Arctic, northwestern Atlantic, and in the Pacific (Figure 16a). The global mean atmospheric $CO_2$ concentration at 1000 hPa in esmHist is about 3.5 ppm higher than in experiment Hist in the last 10 years of the twentieth century.

[60] Consistent with the higher atmospheric $CO_2$ concentration, also the global mean oceanic surface $pCO_2$ is slightly higher in most regions in esmHist. The
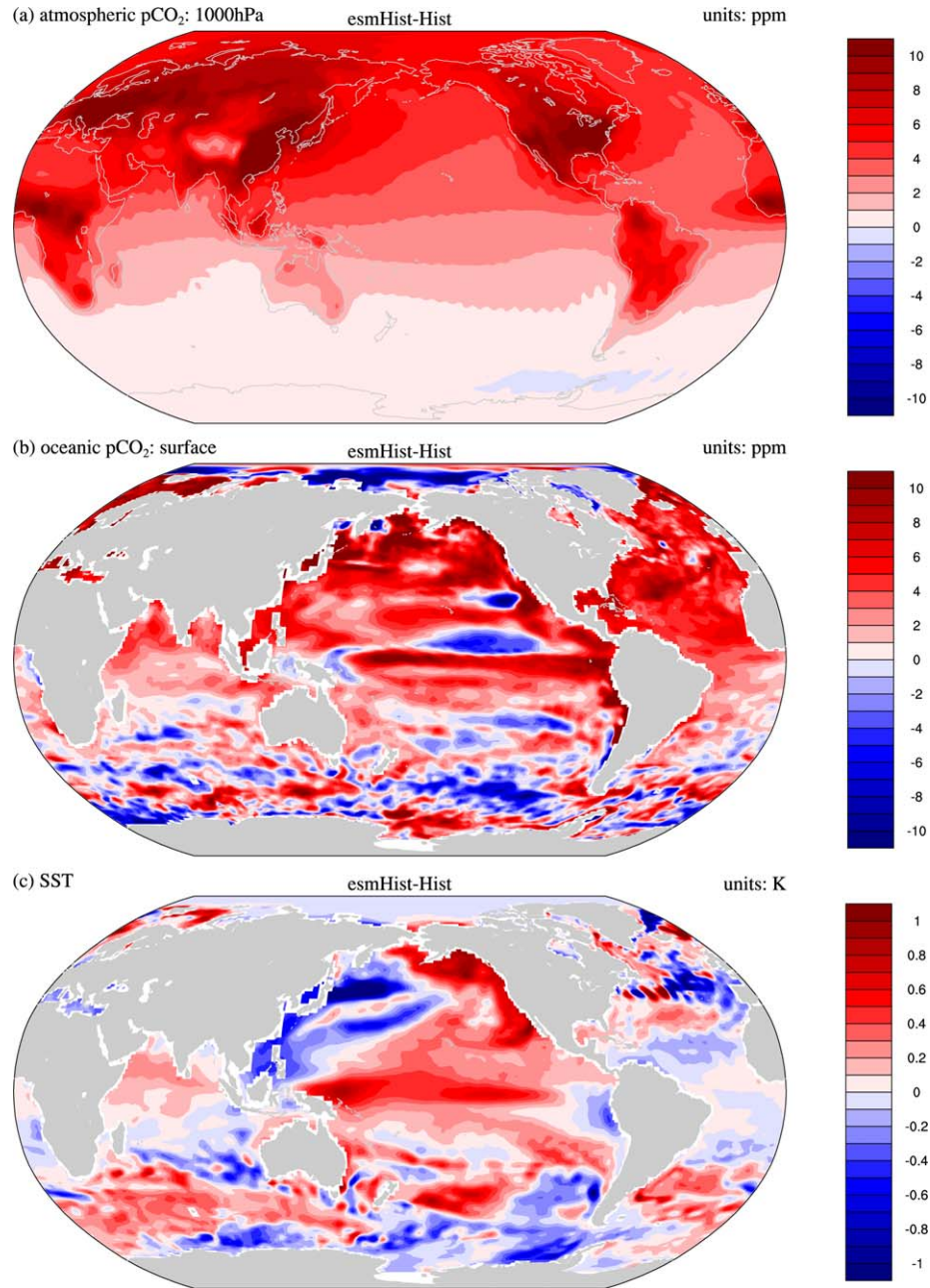
**Figure 16.** Differences of esmHist and Hist experiment calculated as the mean of the years 1991–2000 for (a) atmospheric $CO_2$ concentration at 1000 hPa level, (b) oceanic surface $pCO_2$, and (c) sea surface temperature.

differences between esmHist and Hist in the ocean surface $pCO_2$ (Figure 16b) show more local structures than for atmospheric $pCO_2$ with largest positive anomalies in the North Atlantic and the North Pacific. This may imply a somewhat smaller $CO_2$ uptake by the ocean given smaller sea-air $pCO_2$ difference in the interactive $CO_2$ simulation in these regions. However, this cannot be generalized for the whole ocean, since in the high $pCO_2$ regions such as the EEP and the southern tropical Atlantic, the differences are only weakly positive or even negative. As expected, the difference pattern is patchy in the Southern Ocean where internal variability is large.

[61] The nonuniform distribution of atmospheric $pCO_2$ in esmHist (Figures 16a and 16b) may trigger a different land-sea thermal contrast by trapping more long wave radiation over land, resulting in different atmospheric and oceanic circulation and climate state. The interactive $CO_2$ simulation produces higher SST in the tropical Pacific, northeastern Pacific, and most regions of the Southern Ocean; SST is lower in the mid-latitudes of the North Atlantic, northwestern Pacific,

and some regions of the Southern Ocean (Figure 16c). The global mean SST is slightly (0.05K) higher in the interactive $CO_2$ simulation. These relatively small differences are dominated by the different phasing of the model variability. Various realizations of the esmHist and Hist experiments initialized from different years of the control run (not shown) produce a somewhat different spatial pattern in SST anomalies and in their global mean values (ranging from +0.07K to −0.06K in the different ensemble members, i.e., in the same range as for the difference between esmHist and Hist). Additionally, separate spin-up runs had to be performed for experiments esmHist and Hist leading to slightly different initial conditions in the two historical simulations. Slightly higher temperature in esmHist also leads to an increased soil respiration and net primary production on land providing a positive feedback on atmospheric $pCO_2$ [*Reick et al.*, 2010] (R. Schneck et al., The land contribution to natural $CO_2$ variability on time scales of centuries, submitted to *Journal of Advances in Modeling Earth Systems*, 2012, V. Brovkin et al., Evaluation of vegetation cover and land-surface albedo in MPI-ESM CMIP5 simulations, submitted to *Journal of Advances in Modeling Earth Systems*, 2012). Nevertheless, $CO_2$ forcing during the historical time period is insufficient to override the internal model variability.

[62] The interactive $CO_2$ simulation (esmHist) produces a slightly higher oceanic surface $pCO_2$ throughout the most of the twentieth century beginning around 1940s (Figure 17), with a maximum difference of about 10 ppm in the 1960s. The atmospheric $CO_2$ concentrations in the CMIP5 historical forcing file show nearly constant values around 310 ppm from 1940 to 1950 (not shown) whereas the emissions used to force esmHist rise from 1.34 to 1.58 GtC $yr^{-1}$ over this period. This makes the difference in forcing (rather than the climate-carbon cycle feedbacks) the more likely cause for the deviations between esmHist and Hist. Quite large uncertainties exist in the quantification of these feedbacks. The third Hadley Centre coupled ocean-atmosphere model (HadCM3) for instance produced atmospheric $CO_2$ concentration about 50 ppm higher in an interactive $CO_2$ simulation by 2000 [*Cox et al.*, 2000]. *Fung et al.* [2005] reported a 2 ppm higher atmospheric $CO_2$ concentration in an interactive $CO_2$ simulation by the end of the twentieth century using the National Center for Atmospheric Research-Climate System Model 1 coupled carbon-climate model (NCAR carbon-CSM1.4).

[63] The globally integrated atmosphere to ocean $CO_2$ flux shows a positive trend as the atmospheric $CO_2$ concentration increases. The interannual variability is more prominent in the interactive $CO_2$ simulation: it produces a 25% larger standard deviation than the prescribed atmospheric $pCO_2$ simulation after removal of the 10 year running mean. This indicates higher variability of the model with the free atmospheric $pCO_2$. However, as of today, no evaluation concerning the degree of realism of this variability is available. The ocean takes up more $CO_2$ in the prescribed atmospheric $pCO_2$ simulation in most of the twentieth century
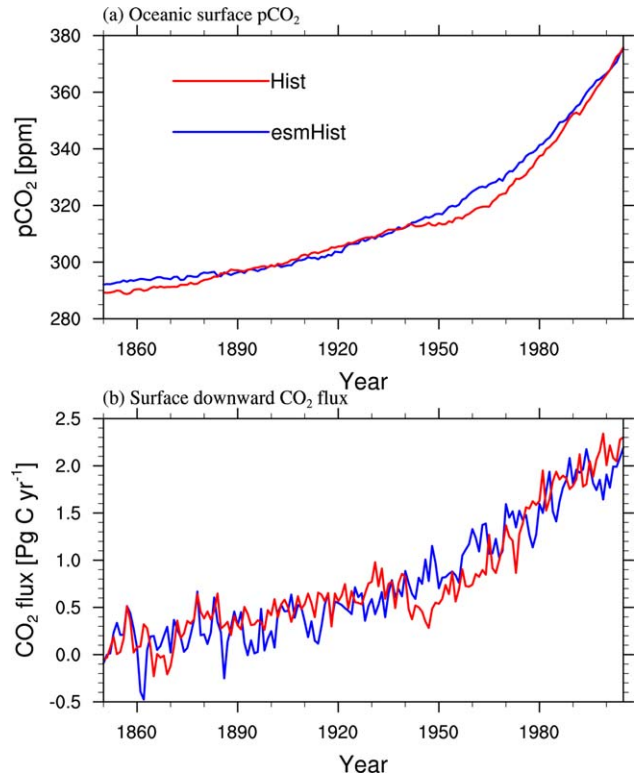


**Figure 17.** Temporal evolution of the (a) global mean oceanic surface $pCO_2$ and (b) surface downward $CO_2$ flux calculated in the experiments esmHist and Hist.

except for the years from 1940 to 1970 when the atmospheric $pCO_2$ is much lower in Hist than in esmHist. The cumulative oceanic $CO_2$ uptake through the whole historical simulation period from year 1850–2005 is 2.59 Pg C larger in the prescribed atmospheric $pCO_2$ simulation.

[64] In summary, the comparison between the esmHist and Hist simulations indicates that the former produces slightly higher near surface atmospheric $CO_2$ concentration and hence a different global temperature and corresponding climate responses. Given the small magnitude of the differences in $pCO_2$ it is, however, difficult to disentangle the changes arising from internal variability of the two simulations, climate-carbon cycle feedbacks, or changes in the forcing.

## 6. Ocean Carbon Cycle in Idealized Experiments

[65] We also evaluated components of the ocean carbon cycle in the idealized CMIP5 experiments (Table 3) including an abrupt 4 × $CO_2$ scenario (in which the atmospheric $pCO_2$ is instantaneously set to four times the preindustrial value, i.e., 1138.9 ppm corresponding to a release of 1811 GtC into the atmosphere and kept at this level for 140 years) and a 1% p.a. scenario (in which the atmospheric $pCO_2$ increases by 1% p.a. until it has reached 4 × $CO_2$, i.e., also 140 years). The main purpose of these experiments within this and earlier CMIPs is to diagnose transient (1% p.a.) and equilibrium (4 × $CO_2$) climate sensitivity, respectively. These

experiments can also be used to evaluate the marine carbon cycle dynamics for a very rapid and a more steady increase in atmospheric $pCO_2$. Furthermore, we discuss the idealized experiments esmFixClim and esmFdbk to give an estimate of the climate- and the $pCO_2$-driven changes in oceanic $CO_2$ uptake, respectively.

[66] Consistent with the experiment setup, the $CO_2$ flux into the ocean is very large at the beginning of the experiment (around 100 GtC yr$^{-1}$) due to the large difference in atmospheric and oceanic $pCO_2$ in the abrupt $4 \times CO_2$ run (hereafter a4×; Figure 18, middle). Already in the second year, the oceanic uptake of carbon is reduced to about 40 GtC yr$^{-1}$, and it drops further over the following 20 years as the oceanic $pCO_2$ increases toward the atmospheric value of 1138.9 ppm. This weakening is additionally enhanced due to increased SST (Figure 18). Oceanic uptake of carbon slowly decreases further being 3 GtC yr$^{-1}$ at the end of the experiment (after 140 years). Note that the response in a4× is to some extent similar to that of a pulse of $CO_2$ in the Earth system but also that it is different in particular for the tail end as the atmospheric $pCO_2$ is kept at $4 \times CO_2$ level.

[67] The time-dependent atmospheric $pCO_2$ concentration is used to force three further experiments (Figure 18): In experiment 1% p.a., both climate and carbon cycle are forced by increasing $pCO_2$. In experiment esmFixClim, only the carbon cycle is forced by increasing $pCO_2$, and in experiment esmFdbk only the climate system is forced by increasing $pCO_2$. In experiment 1% p.a., global $CO_2$ uptake is small at the beginning and increases with time in accordance with the faster rising atmospheric $pCO_2$ towards the end of the experiment. In experiment esmFixClim, where the climate is kept constant at preindustrial level, the uptake rate is larger than in experiment 1% p.a. by about 1 GtC yr$^{-1}$ at the end of the experiment. Finally, in experiment esmFdbk, the change of ocean-atmosphere carbon flux for preindustrial atmospheric $pCO_2$ due to climate change as it would occur under a 1% p.a. increase in atmospheric $pCO_2$ (shown here as increase in global mean SST, Figure 18 bottom) is estimated as an outgassing of about 1 GtC yr$^{-1}$.

[68] Strictly speaking this set of experiments cannot be used to evaluate the climate-carbon cycle feedback, since in none of the experiments the feedback of the climate-induced reduction of oceanic uptake on the atmospheric $pCO_2$ and hence climate is considered. The set of experiments, however, allows quantifying and separating the impact of climate change and atmospheric $pCO_2$ on oceanic carbon uptake. In the above experiments, the atmospheric $pCO_2$ change alone would result in an uptake rate of about 7 GtC yr$^{-1}$, which is reduced by about 1 GtC yr$^{-1}$ due to climate warming, resulting in a combined uptake rate of 6 GtC yr$^{-1}$.

[69] The global values of the integrated primary production over the euphotic zone (INTPP) and the export production at 90 m (EP100) are roughly 61.5 and 9 GtC yr$^{-1}$, respectively (not shown). The internal variability is about 5 GtC yr$^{-1}$ for INTPP and 1 GtC yr$^{-1}$ for EP100. In experiment esmFixClim INTPP and EP100 show no trend over the 140 yrs of the experiment, as the climate is kept constant. In experiment 1% p.a. and esmFdbk, INTPP and EP100 decrease almost linearly in time to a value of 50 GtC yr$^{-1}$ (INTPP) and 7.3 GtC yr$^{-1}$ (EP100). In experiment a4× the decrease of INTPP and EP100 occurs more quickly over the first 25 years: INTPP decreases from 61.5 to about 48 GtC yr$^{-1}$, and EP100 from 9 to 7 GtC yr$^{-1}$. After 25 years, the global integrals of INTPP and EP100 show no further trend. Overall, temporal evolution of INTPP and EP100 in all idealized experiments reflects that of SST (Figure 18) more closely than it does for the $CO_2$ flux.
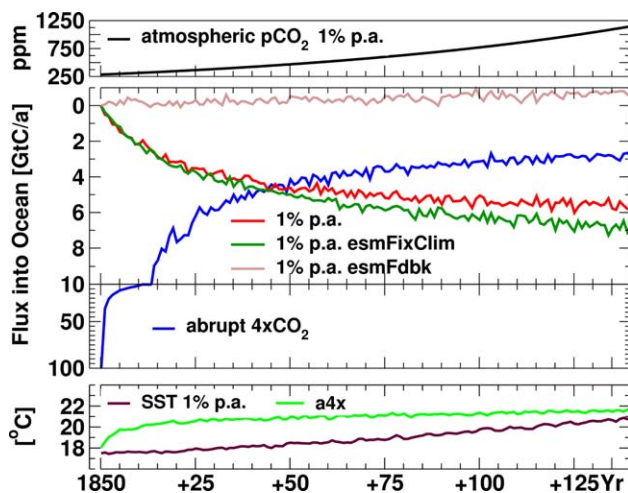
## 7. Summary and Conclusions

[70] In this paper we evaluate the performance of the global ocean biogeochemistry model HAMOCC as component of the MPI-ESM in the framework of different CMIP5 experimental realizations (model version HAMOCC 5.2). HAMOCC 5.2 in CMIP5 experiment "historical" (Hist; Table 3) captures the general observed present day distribution of biogeochemical variables fairly well compared to the available observational database and based on quantitative metrics. The skill of the model to reproduce observations decreases with depth in both configurations (LR and MR) as indicated by quantitative metrics and the Taylor diagrams. An improved horizontal resolution (MR) has a positive impact on model performance in the deeper layers, while the performance at the surface remains almost unchanged. The improvement in the deep layers of the eastern boundary regions in the tropical Pacific and Atlantic in MR indicates a better representation of the interior water mass properties, as well as a better representation of the ocean current systems, i.e., the Agulhas and Equatorial current system (Jungclaus



**Figure 18.** (upper) Atmospheric $CO_2$; (middle) $CO_2$ flux into the ocean (note the reversed vertical axis), and (bottom) sea surface temperature in idealized experiments in 1% p.a. $CO_2$ increase and abrupt quadrupling of $CO_2$ concentrations see Table 3 for details.

et al., submitted manuscript, 2012). The similarities between the surface values in the MR and LR model configurations indicate shortcomings of the atmospheric model, e.g., the overestimation of convection over the warm pool in the tropical Pacific (Stevens et al., submitted manuscript, 2012) and/or the insufficient coupling frequency between the ocean and the atmosphere (once a day; Giorgetta et al., submitted manuscript, 2012). The ACC system tends to produce large deviations between model and observations due to a combination of insufficient representation of the modeled interior water masses (Jungclaus et al., submitted manuscript, 2012) and deficiencies of the ice model (Notz et al., submitted manuscript, 2012). Furthermore, shortcomings due to simple globally tuned formulations of ecosystem processes, vertical fluxes, and oxygen cycle which are common in existing global ocean biogeochemical models [*Schneider et al.*, 2008; *Steinacher et al.*, 2010; *Roy et al.*, 2011; *Cocco et al.*, 2012; *Andrews et al.*, 2012] still persist in HAMOCC regardless of its horizontal resolution.

[71]  We also compared the experiment Hist (see Table 3) forced by prescribed atmospheric $CO_2$ concentrations to the experiment forced by $CO_2$ emissions (interactive carbon cycle; esmHist). This comparison indicates that while being consistent in the representation of the historical evolution of the ocean carbon cycle components, the interactive carbon cycle simulation results overall in slightly higher SST (0.05K), higher (by about 3.5 ppm) atmospheric $pCO_2$ (especially over the Northern Hemisphere), and (up to 10 ppm) higher oceanic $pCO_2$ relative to the experiment forced by prescribed atmospheric $CO_2$ concentrations. These differences are due to different phasing in the internal model variability and lead to only indiscernible variations in the pattern of the oceanic uptake of $CO_2$ between the two experiments over the twentieth century. Additionally, our analysis indicates a 25% higher variability in the $CO_2$ uptake in the free carbon cycle experiment.

[72]  On the contrary, the rate at which atmospheric $CO_2$ concentration increases in idealized experiments (i.e., transient versus abrupt) affects the oceanic carbon sink evolution significantly. While in the transient increase experiment, uptake of atmospheric $CO_2$ by the ocean gradually increases over time, it decreases in the abrupt atmospheric $CO_2$ increase experiment after a sharp initial rise. With regard to the impact of climate warming on the oceanic uptake of $CO_2$, for a 1% p.a. increase in atmospheric $pCO_2$ over 140 years, the induced climate change at the end of the experiment would result in a 1 $GtC\ yr^{-1}$ smaller flux of carbon into the ocean at preindustrial atmospheric $pCO_2$.

[73]  Overall, the model HAMOCC 5.2 performs well as the MPI-ESM's ocean biogeochemistry component. The distribution of model variables and behavior of the modeled processes are consistent between the different model configurations with respect to spatial resolution and the $CO_2$ forcing, being suitable for the type of numerical experiments required within the CMIP5 framework.

# References

Allen, J., J. Holt, J. Blackford, and R. Proctor (2007), Error quantification of a high-resolution coupled hydrodynamic-ecosystem coastal-ocean model: Part 2. Chlorophyll-a, nutrients and spm, *J. Mar. Syst.*, *68*(3-4), 381–404.

Andrews, O. D., N. L. Bindoff, P. R. Halloran, T. Ilyina, and C. Le Quéré (2012), Detecting an external influence on recent changes in oceanic oxygen using an optimal fingerprinting method, *Biogeosci. Discuss.*, *9*(9), 12,469–12,504, doi:10.5194/bgd-9-12469-2012.

Archer, D., and K. Johnson (2000), A model of the iron cycle in the ocean, *Global Biogeochem. Cycles*, *14*(1), 269–279.

Archer, D., M. Lyle, K. Rodgers, and P. Froelich (1993), What controls opal preservation in tropical deep-sea sediments, *Paleoceanography*, *8*(1), 7–21.

Assmann, K. M., M. Bentsen, J. Segschneider, and C. Heinze (2010), An isopycnic ocean carbon cycle model, *Geosci. Model Dev.*, *3*(1), 143–167, doi:10.5194/gmd-3-143-2010.

Aumont, O., E. Maier-Reimer, S. Blain, and P. Monfray (2003), An ecosystem model of the global ocean including Fe, Si, P colimitations, *Global Biogeochem. Cycles*, *17*(2), 1060, doi:10.1029/2001GB001745.

Bacastow, R., and E. Maier-Reimer (1990), Ocean—Circulation model of the carbon cycle, *Clim. Dyn.*, *4*, 95–125.

Bhattacharyya, A. (1943), On a measure of divergence between two statistical populations defined by their probability distributions, *Bull. Calcutta Math. Soc.*, *35*, 99–109.

Broecker, W., and T. Peng (1982), *Tracers in the Sea*, Lamont-Doherty Geol. Observatory, Columbia Univ.

Brovkin, V., S. Lorenz, J. Jungclaus, T. Raddatz, C. Reick, C. Timmreck, J. Segschneider, and K. Six (2010), Sensitivity of a coupled climate-carbon cycle model to large volcanic eruptions during the last millennium. *Tellus B*, *62*(5), 674–681.

Cocco, V., et al. (2012), Oxygen and indicators of stress for marine life in multi-model global warming projections, *Biogeosci. Discuss.*, *9*(8), 10,785–10,845, doi:10.5194/bgd-9-10785-2012.

Cox, P., and C. Jones (2008), Illuminating the modern dance of climate and $CO_2$, *Science*, *321*(5896), 1642–1644, doi:10.1126/science.1158907.

Cox, P., R. Betts, C. Jones, S. Spall, and I. Totterdell (2000), Acceleration of global warming due to carbon-cycle feedbacks in a coupled climate model, *Nature*, *408*(6809), 184–187.

Duteil, O., et al. (2012), Preformed and regenerated phosphate in ocean general circulation models: Can right total concentrations be wrong?, *Biogeosciences*, *9*(5), 1797–1807, doi:10.5194/bg-9-1797-2012.

Eppley, R. W. (1972), Temperature and phytoplankton growth in the sea, *Fish. Bull.*, *70*, 1063–1085.

Friedlingstein, P., et al. (2006), Climate–carbon cycle feedback analysis: Results from the C4MIP model intercomparison, *J. Clim.*, *19*(14), 3337–3353, doi:10.1175/JCLI3800.1.

Fung, I., S. Doney, K. Lindsay, and J. John (2005), Evolution of carbon sinks in a changing climate, *Proc. Natl. Acad. Sci. U. S. A.*, *102*(32), 11,201–11,206.

Garcia, H. E., R. A. Locarnini, T. P. Boyer, J. I. Antonov, O. K. Baranova, M. M. Zweng, and D. R. Johnson (2010a), World ocean atlas 2009, vol. 3: Dissolved oxygen, apparent oxygen utilization, and oxygen saturation, *Technical Report*, U.S. Gov. Print. Off., Washington, D. C., NOAA Atlas NESDIS 70.

Garcia, H. E., R. A. Locarnini, T. P. Boyer, J. I. Antonov, M. M. Zweng, O. K. Baranova, and D. R. Johnson (2010b), World ocean atlas 2009, vol. 4: Nutrients (phosphate, nitrate, silicate), *Technical Report*, U.S. Gov. Print. Off., Washington, D. C., NOAA Atlas NESDIS 71.

Goyet, C., and A. Poisson (1989), New determination of carbonic acid dissociation constants in seawater as a function of temperature and salinity, *Deep Sea Res. A. Oceanograph. Res. Pap.*, *36*(11), 1635–1654, doi:10.1016/0198-0149(89)90064-2.

Gröger, M., and U. Mikolajewicz (2011), Note on the $CO_2$ air-sea gas exchange at high temperatures, *Ocean Modell.*, *39*, 284–290.

Heinze, C. (2004), Simulating oceanic $CaCO_3$ export production in the greenhouse, *Geophys. Res. Lett.*, *31*, L16308, doi:10.1029/2004GL026013.

Heinze, C., and E. Maier-Reimer (1999), The Hamburg oceanic carbon cycle circulation model version "HAMOCC2s" for long time integrations, *Tech. Rep. 20*, Deutsches Klimarechenzentrum, Modellbetreuungsgruppe, Hamburg, Germany.

Heinze, C., E. Maier-Reimer, A. M. E. Winguth, and D. Archer (1999), A global oceanic sediment model for long-term climate studies, *Global Biogeochem. Cycles*, *13*(1), 221–250, doi:10.1029/98GB02812.

Heinze, C., A. Hupe, E. Maier-Reimer, N. Dittert, and O. Ragueneau (2003), Sensitivity of the marine biospheric Si cycle for biogeochemical parameter variations, *Global Biogeochem. Cycles*, *17*(3), 1086, doi:10.1029/2002GB001943.

Ilyina, T., and R. E. Zeebe (2012), Detection and projection of carbonate dissolution in the water column and deep-sea sediments due to ocean acidification, *Geophys. Res. Lett.*, *39*(6), doi:10.1029/2012GL051272, L06606.

Ilyina, T., R. E. Zeebe, E. Maier-Reimer, and C. Heinze (2009), Early detection of ocean acidification effects on marine calcification, *Global Biogeochem. Cycles*, *23*(1), doi:10.1029/2008GB003278, GB1008.

Ilyina, T., R. Zeebe, and P. Brewer (2010), Future ocean increasingly transparent to low-frequency sound owing to carbon dioxide emissions, *Nat. Geosci.*, *3*(1), 18–22.

Jassby, A. D., and T. Platt (1976), Redfield ratio based on chemical data from isopycnal surfaces, *Limnol. Oceanogr.*, *21*, 540–547.

Jungclaus, J., N. Keenlyside, M. Botzet, H. Haak, J. Luo, M. Latif, J. Marotzke, U. Mikolajewicz, and E. Roeckner (2006), Ocean circulation and tropical variability in the coupled model ECHAM5/MPI-OM, *J. Clim.*, *19*(16), 3952–3972.

Jungclaus, J. H., et al. (2010), Climate and carbon-cycle variability over the last millennium, *Clim. Past Discuss.*, *6*(3), 1009–1044, doi:10.5194/cpd-6-1009-2010.

Keeling, R., B. Stephens, R. Najjar, S. Doney, D. Archer, and M. Heimann (1998), Seasonal variations in the atmospheric $O_2/N_2$ ratio in relation to the kinetics of air-sea gas exchange, *Global Biogeochem. Cycles*, *12*(1), 141–163.

Key, R., et al. (2004), A global ocean carbon climatology: Results from global data analysis project (GLODAP), *Global Biogeochem. Cycles*, *18*(4), GB4031, doi:10.1029/2004GB002247.

Kloster, S., J. Feichter, E. Maier-Reimer, K. D. Six, P. Stier, and P. Wetzel (2006), DMS cycle in the marine ocean-atmosphere system—A global model study, *Biogeosciences*, *3*(1), 29–51, doi:10.5194/bg-3-29-2006.

Kloster, S., K. D. Six, J. Feichter, E. Maier-Reimer, E. Roeckner, P. Wetzel, P. Stier, and M. Esch (2007), Response of dimethylsulfide (DMS) in the ocean and atmosphere to global warming, *J. Geophys. Res.*, *112*(G3), G03005, doi:10.1029/2006JG000224.

Le Clainche, Y., et al. (2010), A first appraisal of prognostic ocean DMS models and prospects for their use in climate models, *Global Biogeochem. Cycles*, *24*, GB3021, doi:10.1029/2009GB003721

Locarnini, R. A., A. V. Mishonov, J. I. Antonov, T. P. Boyer, H. E. Garcia, O. K. Baranova, M. M. Zweng, and D. R. Johnson (2010), World ocean atlas 2009, vol. 1: Temperature, *Tech. Rep. 1*, U.S. Gov. Print. Off., Washington, D. C.

Lochte, K., H. Ducklow, M. Fasham, and C. Stienen (1993), Plankton succession and carbon cycling at 47 N 20 W during the JGOFS North Atlantic Bloom Experiment, *Deep Sea Res. Part II*, *40*(1), 91–114.

Mahowald, N., M. Yoshioka, W. Collins, A. Conley, D. Fillmore, and D. Coleman (2006), Climate response and radiative forcing from mineral aerosols during the last glacial maximum, pre-industrial, current and doubled-carbon dioxide climates, *Geophys. Res. Lett*, *33*(20), L20705, doi:10.1029/2003GL017880.

Maier-Reimer, E. (1984), Towards a global ocean carbon model, *Progr. Biometeorol.*, *3*, 295–310.

Maier-Reimer, E. (1993), Geochemical cycles in an ocean general circulation model. Preindustrial tracer distributions, *Global Biogeochem. Cycles*, *7*, 645–677.

Maier-Reimer, E., and K. Hasselmann (1987), Transport and storage of $CO_2$ in the ocean—An inorganic ocean-circulation carbon cycle model, *Clim. Dyn.*, *2*, 63–90.

Maier-Reimer, E., U. Mikolajewicz, and K. Hasselmann (1993), Mean circulation of the Hamburg LSG OGCM and its sensitivity to the thermohaline surface forcing, *J. Phys. Oceanogr.*, *23*, 731–757.

Maier-Reimer, E., I. Kriest, J. Segschneider, and P. Wetzel (2005), The Hamburg oceanic carbon cycle circulation model HAMOCC5.1—Technical Description Release 1.1, *Tech. Rep. 14*, Reports on Earth System Science, Max Planck Institute for Meteorology, Hamburg, Germany.

Maréchal, F., S. Leuenberger, Y. Membrez, O. Bucheli, D. Favrat, et al. (2004), Process flow model of solid oxide fuel cell system supplied with sewage biogas, *J. Power Sources*, *131*(1), 127–141.

Monteiro, F., M. Follows, and S. Dutkiewicz (2010), Distribution of diverse nitrogen fixers in the global ocean, *Global Biogeochem. Cycles*, *24*(3), GB3017, doi:10.1029/2009GB003731.

Moss, R., et al. (2010), The next generation of scenarios for climate change research and assessment, *Nature*, *463*(7282), 747–756.

Najjar, R., et al. (2007), Impact of circulation on export production, dissolved organic matter, and dissolved oxygen in the ocean: Results from phase ii of the ocean carbon-cycle model intercomparison project (OCMIP-2), *Global Biogeochem. Cycles*, *21*(3), GB3007, doi:10.1029/2006GB002857.

Orr, J., et al. (2005), Anthropogenic ocean acidification over the twenty-first century and its impact on calcifying organisms, *Nature*, *437*(7059), 681–686.

Parekh, P., M. Follows, and E. Boyle (2005), Decoupling of iron and phosphate in the global ocean, *Global Biogeochem. Cycles*, *19*(2), GB2020, doi:10.1029/2004GB002280.

Reick, C., T. Raddatz, J. Pongratz, and M. Claussen (2010), Contribution of anthropogenic land cover change emissions to pre-industrial atmospheric $CO_2$, *Tellus B*, *62*(5), 329–336.

Roeckner, E., M. Giorgetta, T. Crueger, M. Esch, and J. Pongratz (2011), Historical and future anthropogenic emission pathways derived from coupled climate–carbon cycle simulations, *Clim. Change*, *105*(1), 91–108.

Roy, T., et al. (2011), Regional impacts of climate change and atmospheric $CO_2$ on future ocean carbon uptake: A multi-model linear feedback analysis, *J. Clim.*, *24*, 2300–2318.

Schneider, B., et al. (2008), Climate-induced interannual variability of marine primary and export production in three global coupled climate carbon cycle models, *Biogeosciences*, *5*(2), 597–614, doi:10.5194/bg-5–597-2008.

Segschneider, J., A. Beitsch, C. Timmreck, V. Brovkin, T. Ilyina, J. Jungclaus, S. J. Lorenz, K. D. Six, and D. Zanchettin (2013), Impact of an extremely large magnitude volcanic eruption on the global climate and carbon cycle estimated from ensemble Earth System Model simulations. *Biogeosciences*, *10*, 669–687, doi:10.5194/bg-10-669-2013.

Six, K. D., and E. Maier-Reimer (1996), Effects of plankton dynamics on seasonal carbon fluxes in an ocean general circulation model, *Global Biogeochem. Cycles*, *10*, 559–583.

Six, K. D., and E. Maier-Reimer (2006), What controls the oceanic dimethylsulfide (DMS) cycle? A modeling approach, *Global Biogeochem. Cycles*, *20*, GB4011, doi:10.1029/2005GB002674.

Smith, E. (1936), Photosynthesis in relation to light and carbon dioxide, *Proc. Natl. Acad. Sci. U. S. A.*, *22*(8), 504–511.

Steinacher, M., et al. (2010), Projected 21st century decrease in marine productivity: A multi-model analysis, *Biogeosciences*, *7*(3), 979–1005.

Stow, C., J. Jolliff, D. McGillicuddy, S. Doney, J. Allen, M. Friedrichs, K. Rose, and P. Wallhead (2009), Skill assessment for coupled biological/physical models of marine systems, *J. Mar. Syst.*, *76*(1), 4–15.

Takahashi, T., W. S. Broecker, and S. Langer (1985), Redfield ratio based on chemical data from isopycnal surfaces, *J. Geophys. Res.*, *90*(C4), 6907–6924.

Takahashi, T., et al. (2002), Global sea-air $CO_2$ flux based on climatological surface ocean pCO2, and seasonal biological and temperature effects, *Deep Sea Res. Part II*, *49*(9-10), 1601–1622.

Takahashi, T., et al. (2009), Climatological mean and decadal change in surface ocean pCO2, and net sea-air $CO_2$ flux over the global oceans, *Deep Sea Res. Part II*, *56*(8-10), 554–577.

Taylor, K. (2001), Summarizing multiple aspects of model performance in a single diagram, *J. Geophys. Res*, *106*(D7), 7183–7192.

Taylor, K., R. Stouffer, and G. Meehl (2011), An overview of CMIP5 and the experiment design, *Bull. Am. Meteorol. Soc.*, *93*(4), 485–498.

Tjiputra, J. F., C. Roelandt, M. Bentsen, D. M. Lawrence, T. Lorentzen, J. Schwinger, Ø. Seland, and C. Heinze (2012), Evaluation of

the carbon cycle components in the Norwegian Earth system model (NORESM), *Geosci. Model Dev. Discuss.*, *5(4)*, 3035–3087, doi:10.5194/gmdd-5–3035-2012.

Wanninkhof, R. (1992), Relationship between wind speed and gas exchange, *J. Geophys. Res*, *97*(25), 7373–7382.

Weiss, R. (1970), The solubility of nitrogen, oxygen and argon in water and seawater, in *Deep Sea Research and Oceanographic Abstracts*, vol. *17*, pp. 721–735, Elsevier, doi:10.1016/0011-7471(70)90037-9.

Weiss, R. (1974), Carbon dioxide in water and seawater: The solubility of a non-ideal gas, *Mar. Chem.*, *2*(3), 203–215.

Wetzel, P., A. Winguth, and E. Maier-Reimer (2005), Sea-to-air $CO_2$ flux from 1948 to 2003: A model study, *Global Biogeochem. Cycles*, *19*(2), GB2005, doi:10.1029/2004GB002339.

Winguth, A. M. E., M. Heinmann, K. D. Kurz, E. Maier-Reimer, U. Mikolajewicz, and J. Segschneider (1994), El Niño-Southern Oscilla-

tion related fluctuations of the marine carbon cycle, *Global Biogeochem. Cycles*, *8*(1), 39–63, doi:10.1029/93GB03134.

Zeebe, R., and D. Wolf-Gladrow (2001), *$CO_2$ in Seawater: Equilibrium, Kinetics, Isotopes*, vol. *65*, Elsevier.

Zielinski, O., O. Llinás, A. Oschlies, and R. Reuter (2002), Underwater light field and its effect on a one-dimensional ecosystem model at station ESTOC, north of the Canary Islands, *Deep Sea Res. Part II*, *49*(17), 3529–3542, doi:10.1016/S0967-0645 (02)00096-6.

Corresponding author: T. Ilyina, Max Planck Institute for Meteorology, Bundesstr. 53, D-20146 Hamburg, Germany. (tatiana.ilyina@z-maw.de)